Green Synthesis of Fe_3O_4 Nanoparticles Using *Eucalyptus Globules Leaf* Extract and Its Application for Phosphate Removal from Synthetic Wastewater

By:Gemechis Asfaw

A Thesis Submitted To the Department of Applied Chemistry

School of Applied Natural Science

Presented in Partial Fulfillment of the Requirements for the Degree of Master's in Chemistry (Industrial Chemistry)

Office of Graduate Studies

Adama Science and Technology University

August 2021

Adama, Ethiopia

Green Synthesis of Fe_3O_4 Nanoparticles Using *Eucalyptus Globules Leaf* Extract and Its Application for Phosphate Removal from Synthetic Wastewater

By:Gemechis Asfaw

Advisor: Dr.Bedasa Abidisa

A Thesis Submitted To the Department of Applied Chemistry

School of Applied Natural Science

Presented in Partial Fulfillment of the Requirements for the Degree of Master's in Chemistry (Industrial Chemistry)

Office of Graduate Studies

Adama Science and Technology University

August 2021

Adama, Ethiopia

Approval of Board of Evaluators

I the advisors of the thesis entitled "Green Synthesis of Fe_3O_4 Nanoparticles Using *Eucalyptus Globules Leaf* Extract and Its Application for Phosphate Removal from Synthetic Wastewater" and developed by Gemechis Asfaw hereby certify that the recommendation and suggestions made by the board of examiners are appropriately incorporated into the final version of the thesis.

Name of major Advisor	Signature	Date

We, the undersigned, members of the Board of Examiners of the thesis by Gemechis Asfaw have read and evaluated the thesis entitled "Green Synthesis of Fe_3O_4 Nanoparticles Using *Eucalyptus Globules Leaf* Extract and Its Application for Phosphate Removal from Synthetic Wastewater " and examined the candidate during open defense. This is, therefore, to certify that the thesis is accepted for partial fulfillment of the requirement of the degree of Master of Science in Industrial Chemistry.

Chairperson	Signature	Date
Internal Examiner	Signature	Date
External Examiner	Signature	Date

Final approval and acceptance of the thesis is contingent upon submission of its final copy to the Office of Postgraduate Studies (OPGS) through the Department Graduate Council (DGC) and School Graduate Committee (SGC).

Department Head	Signature	Date
School Dean	Signature	Date
Office of Postgraduate Studies	Dean Signature	Date

Declaration

I hereby declare that this Master Thesis entitled "Green Synthesis of Fe_3O_4 Nanoparticles Using *Eucalyptus Globules Leaf* Extract and Its Application for Phosphate Removal from Synthetic Wastewater" submitted to Adama Science and Technology University is my original work. That is, it has not been submitted for the award of any academic degree, diploma or certificate in any other university. All sources of materials that are used for this thesis have been duly acknowledged through citation.

Name of Student	Signature	Date

APPROVAL SHEET

To: Applied Chemistry Department

Subject: M.Sc Thesis Submission

This is to certify that the M.Sc thesis entitled "Green Synthesis of Fe_3O_4 Nanoparticles Using *Eucalyptus Globules Leaf* Extract and Its Application for Phosphate Removal from Synthetic Wastewater" submitted in partial fulfillment of the requirements for the degree of Master's in Science, the Graduate program of the department of Applied Chemistry, and has been carried out by Gemechis Asfaw Id. No PGE/18689/11, under my supervision. Therefore, I recommend that the student has fulfilled the requirements and hence hereby he can submit the thesis to the department.

Name of Student	Signature	Date
Name of major Advisor	Signature	Date

ACKNOWLEDGMENT

First of all I would like to thank almighty God for helping me to complete my research work successfully.

Then I would like to express my heartfelt gratitude to my advisor, Dr. Bedasa Abdisa for his guidance & technical support in this research. I would like to acknowledge the department of Applied Chemistry for facilitating all the things to complete this research. I have also special thanks to chemistry laboratory lab assistances for their help during laboratory experiment and I would like to express my thanks to the department of Applied Biology for their help during UV visible spectroscopy analysis of laboratory work.

Finally I have special and deepest appreciations for my mom Tsige Terefe Weyesa who made me believe in myself and encouraged me through the whole process of research.

Table of Contents

LIST OF TABLE

LIST OF FIGURE

LIST OF ABBREVIATION

MNP …….Magnetic Nanoparticle

EBPR……Enhanced biological phosphorus removal

EGLE……*Eucalyptus Globules* leaf extract

GAOs……Glycogen Accumulating Organisms

PAOs……Polyphosphate Accumulating Organisms

PHA……..Polyhydroxy Alkanoates

pH_{PZC} .....pH of point of zero charge

FTIR…….Fourier Transform Infrared Spectroscopy

XRD…….X-Ray Diffraction

TGA…….Thermogravimetric analysis

SEM…….Scanning Electron Microscopy

UV-VIS……Ultraviolet-Visible Light Spectroscopy

DRS……..Diffuse reflectance spectroscopy

WWT…….Waste Water Treatment

NPs.……Nanoparticles

ABSTRACT

Phosphorus concentrations typically are low in natural waters, but it is required in relatively large amounts by plants. Phosphorus is generally the most important nutrient controlling plant growth in aquatic ecosystems, and also phosphorus pollution of natural waters is considered a primary cause of eutrophication. In this research work, EGLE coated magnetite nanoparticles at volume ratio of 2:1, 1:1, and 1:2 were synthesized with the same method by varying the proportion of precursor and EGLE in presence of NaOH by co- precipitation process. The synthesized NPs were characterized by using TGA, XRD, FTIR, DRS, and SEM analysis. The characterized nanoparticles were used for the removal of phosphate from aqueous solution by adsorption mechanism and all the adsorption experiments were carried out in batch mode. The effects of the contact time, dose of the adsorbent, pH, and initial phosphate concentration on the adsorption capacity were studied. The crystal size of the synthesized NPs calculated by Debye-Scherer equation were 10.7 nm, 14.34 nm and 14.79 nm for 2:1, 1:1 and 1:2 NPs respectively. The band gap energy of synthesized NPs was found to be 2.19 eV, 1.92 eV and 1.89 eV for 2:1, 1:1 and 1:2 NPs respectively. The results showed that the adsorption capacity for the phosphate increased by increasing the contact time, adsorbent dose at pH=6 of the solution. The adsorption kinetics was in good agreement with pseudo 2^{nd} order kinetic equation and the adsorption isotherm showed good fitting to Freundlich isotherm. The phosphate removal efficiency of 2:1, 1:1 and 1:2 Fe_3O_4-EGLE NPs were 98.97%, 97.32% and 97.50%, respectively. The results suggested that the biosynthesized Fe_3O_4 nanoparticles using EGLE displayed a definitive potential for phosphate removal from synthetic wastewater.

Keywords: Eucalyptus Globules, Co-Precipitation, Magnetite Nanoparticles, Adsorption

CHAPTER ONE

1. Introduction

1.1 Background of the Study

The management of water resources is one of the most challenging problems faced at local and global levels. The water circuit has implications for both the availability of clean water sources for human consumption as well as for the normal functioning of natural ecosystems. Human activities and advances in industrial and agricultural processes have greatly affected the quality of water resources and impacted the nutrient cycle, which is essential for all forms of life. The main effects are observed in the nitrogen (N) ˉ and phosphorus (P)ˉcycles in the ecosystem, two elements that are vital for living organisms. P is part of the building blocks of cells and plays an important role in bioenergetics processes and in the storage and processing of genetic information (Ali Othman, 2018).

Phosphorus exists in natural waters in particulate and dissolved form. It is known that phosphorus is essential to the growth of algal and other biological organisms. Because of algal blooms that occur in surface waters, the amount of phosphorus compounds in domestic and industrial discharges must be controlled using either chemical or biological techniques. The usual forms of phosphorus found in aqueous solutions include orthophosphates, polyphosphates and organic phosphates. The principal phosphorus compounds in wastewater are generally orthophosphates. Municipal wastewater may contain from 4 to 15 mg/L phosphorus as $PO4^{3-}$. However, industrial wastewaters (such as detergent manufacturing and metal coating processes) may contain phosphate levels well in excess of 10 mg/L (N. Yeddou Mezenner, 2010).

Excessive phosphates present in natural waters are known to cause eutrophication. One of the signs of eutrophication is dense algal blooms that cause high turbidity in aquatic systems, decreasing dissolved oxygen and increasing hypoxia conditions in the deeper parts of water bodies because of plant decay in sediments. In addition, floating algal blooms, known as blue-green algae, formed in freshwaters is another symptom of nutrient excess, which is caused by nitrogen-fixing cyanobacteria. Dissolved phosphate of ~ 0.02 mg/L is considered to have

potential to lead to profuse algal growth in waters which will in turn deplete the oxygen further leading to poor water quality (Motlagh, 2014).

Various techniques have been are applied for phosphate removal, such as chemical precipitation, adsorption, and biological processes. However, biological processes are unreliable because the quality of water has a significant impact on phosphate removal. Chemical precipitation often consumes a large amount of coagulant but requires sludge treatment and material disposal. Nowadays, Adsorption is an alternative and promising phosphate removal method, especially for wastewater with a low phosphate concentration, due to the production of less sludge, easy operation, and high efficiency (Jeongyun Choi J. C., 2016).

In recent years, iron based nanoparticles have been widely applied for environmental remediation as adsorbant. The strong magnetic properties of such nanoparticles enable separation of adsorbent and adsorbate by using a simple magnet. Magnetite, an iron (Fe_3O_4) material shows the highest magnetism among all the naturally available minerals. Application of bare magnetite nanoparticles (MNP) for the removal of toxic water contaminants have been reported into the literature. However, the susceptibility to auto-oxidation, tendency to agglomeration and concerns over toxicity are the main challenges for the real life water treatment applications of bare MNP. The coating of natural organic matter (NOM) on the bare MNP surface has been found useful in making the nanoparticles less toxic and more environmental friendly. Such thin coatings can also inhibit the agglomeration and auto-oxidation; the primary drawbacks associated with the use of bare MNP (Mamun Rashid N. T., 2017).

(Jaison Jeevanandam, 2018) reported that Eucalyptus oil and phenols are the major phytochemical components that are found *Eucalyptus Globules* leaf extract. Besides, phytochemicals such as tannins, saponins, flavonoids, reducing sugars, glycosides and terpenoids that are essential in the Stabilizing and coating of metal ions are also present in the leaf extract of *Eucalyptus Globules leaf extract*. Given the fact that *Eucalyptus Globules* leaf is abundantly available and the use of Eucalyptus leaves for green synthesis of Fe_3O_4 NPs benefits resource recycling and reduces production cost of Fe_3O_4 NPs as well as

environmental risk, study on green synthesis of Fe_3O_4 NPs using *Eucalyptus Globules* leaf extract is required, and hence the green synthesized Fe_3O_4 NPs used for phosphate removal is a potential application in environmental remediation.

1.2 Statement of the problem

Contamination of water is a widespread problem throughout the world as a result of pollution. One of the most important pollutants in water is the excess of nutrients (nitrogen and phosphorus) that threatens human health and the environment. Phosphorus is the limiting nutrient for algae (autotrophic) growth in most fresh water bodies (lakes, rivers and reservoirs) and some coastal waters influenced by river discharges. The anthropogenic discharge of phosphorus to these waters therefore increases the potential for algae growth, which is the starting point of eutrophication (Helmut Kroiss, 2011). A variety of physical, chemical, and biological methods have been developed in recent years for the removal of phosphate from wastewater. Advanced biological methods can remove up to 97% of phosphate and generate low amounts of sludge but the method has limited practical applicability. Similarly, physical processes (sedimentation, membrane filtration, etc.) techniques are too expensive and accompanied by a high sludge production and often inefficient in the removal of phosphate from wastewater effluent (Khan.S., 2013).

According to (Manahan, 2017) municipal wastewater typically contains approximately 25 mg/L of phosphate (as orthophosphates, polyphosphates, and insoluble phosphates) but Algae may grow at $PO4^{3-}$ levels as low as 0.5 mg/L. Therefore, sufficient removal of phosphate is required. This research intended to synthesize cost effective and environmentally friendly method Fe_3O_4 nanoparticles Using *Eucalyptus Globulus* leaf extract and analyze Its Application for Phosphate Removal from Synthetic Wastewater. Furthermore, the possibility of phosphorus recovery and its efficiency depending on magnetite properties was studied.

1.3 Objectives

1.3.1 General objective

The general objective of this proposal was synthesizing magnetite nanoparticles using eucalyptus leaf extract by co-precipitation method and applying the nanomaterial for the removal and recovery of phosphorus from synthetic wastewater.

1.3.2 Specific objectives

The specific objectives of this work were:

- To synthesize Fe_3O_4 NPs using leaf extract of *Eucalyptus Globulus* leaf extract
- To characterize the synthetic Fe_3O_4 nanoparticles using UV-Vis, XRD, SEM, FTIR, and TGA
- To evaluate phosphate removal efficiency of the synthesized Fe_3O_4 nanoparticles from wastewater
- To carry out adsorption isotherm and kinetics studies of Fe_3O_4 nanoparticles

1.4 Significance of the study

This study will provide important information about Synthesis of Fe_3O_4 Using *Eucalyptus Globulus* leaf extract by co-precipitation method and would also be used as a base for further research in this area for interested researchers.

1.5 The Scope Of the study

The study will cover about synthesis of Fe_3O_4 nanoparticle using *Eucalyptus Globulus* leaf extract in co-precipitation method, the characterization of this nanoparticle using UV-Vis, FTIR, XRD, SEM, & TGA technique and its application for removal of phosphate ion from synthetic wastewater.

CHAPTER TWO

2. Literature Review

2.1 Origins of phosphate in water bodies

Phosphorus (P) is a key element for all living systems. Phosphorus is a component of DNA and RNA and indispensable for the energetic metabolism (ADP/ATP) of living beings. Phosphorus cannot be substituted in these biological functions by any other element (Ruttenberg, 2001). The tremendous growth of global population is therefore linked to a proportional increase of phosphorus requirement for the production of food, which actually to a large extent is depending on the use of mineral phosphorus fertiliser. Many natural (aquatic) ecosystems are controlled by restricted availability of phosphorus which represents one important factor for high biodiversity. The anthropogenic increase of phosphorus flows therefore has the potential to cause severe negative effects on natural (aquatic) ecosystems (Taylor, 2018).

Phosphorus concentrations typically are low in natural waters, but it is required in relatively large amounts by plants. Phosphorus is generally the most important nutrient controlling plant growth in aquatic ecosystems, and also phosphorus pollution of natural waters is considered a primary cause of eutrophication. Phosphorus is absorbed strongly by bottom sediment where it is bound in iron, aluminum, and calcium phosphate compounds and adsorbed onto iron and aluminum oxides and hydroxides. The solubility of the mineral forms is regulated by pH, and there are few situations in nature in which phosphorus minerals are highly soluble (Helmut Kroiss, 2011).The phosphorus in organic matter is mineralized, but when it is, it usually will be adsorbed by sediment unless it is quickly absorbed by plants or bacteria. Because sediment tends to be a sink for phosphorus, high rates of plant growth in aquatic ecosystems require a continuous input of phosphorus. Phosphorus has several valence states ranging from +3 to +5, but most phosphorus found in nature has a valence state of +5. In contrast with nitrogen and sulfur, oxidation and reduction reactions mediated by chemotropic bacteria are not an important feature of its cycle. Despite its tremendous biological importance, the phosphorus cycle is largely a chemical cycle instead of a biologically-driven one. Of course, microbial

decomposition is an important factor in releasing phosphorus from organic matter (Boyd, 2015).

There are three main ways of how phosphates enter wastewater and ground water this are leaching from the natural mineral deposits; Agriculture; Sewage disposal and liquid urban waste (domestic and industrial) (Loganathan, 2013). Phosphorus is found in dissolved or particulate form. Dissolved phosphorus in soils, sediment, and water normally can be considered an ionization product of orthophosphoric acid (H_3PO_4) that dissociates into di-orthophosphate,mono-orthophosphate,and phosphate as follows:

$$H_3PO_4 = H^+ + H_2PO_4^- \qquad K_1 = 10^{-2.13} \ldots\ldots\ldots\ldots\ldots\ldots (1)$$

$$H_2PO_4 = H^+ + HPO_4^- \qquad K_2 = 10^{-7.21} \ldots\ldots\ldots\ldots\ldots\ldots\ldots (2)$$

$$HPO_4^{2-} = H^+ + PO_4^{3-} \qquad K_3 = 10^{-12.36} \ldots\ldots\ldots\ldots\ldots\ldots (3)$$

There is no un-ionized H_3PO_4 except in highly acidic solutions, and $PO4^{3-}$ predominates only in highly basic solutions. Within the pH range of most natural waters, dissolved phosphate will exist as $H_2PO_4^-$ and HPO_4^{2-}. At pH values below 7.21, there will be more $H_2PO_4^-$, and HPO_4^{2-}will dominate at pH 7.22 and above (Boyd, 2015).

Orthophosphate concentrations in natural environments are very low in the order of 10 µg phosphorus/liter (in the case of alpine lakes or pelagic marine waters). In environments highly disturbed by human activities, they can reach several hundred µg phosphorus/liter (Wetzel, 2001).Figure 1 shows effect of pH on relative proportion of different forms of phosphate. Particulate phosphorus, the Organic fraction corresponds to all the phosphates of organic animal and vegetable matter, living or in the process of mineralization. It can represent a significant part of particulate phosphorus: up to 50% in river sediments in agricultural areas for example. The Inorganic fraction can be present in two forms; crystalline phosphorus (calcium, iron or aluminum salts) which is among the least soluble forms and phosphorus fixed or adsorbed on the surface of the particles and its constituents (calcium carbonate, iron and aluminum hydroxides, clay, organic matter) (Dekun Hou, 2013).

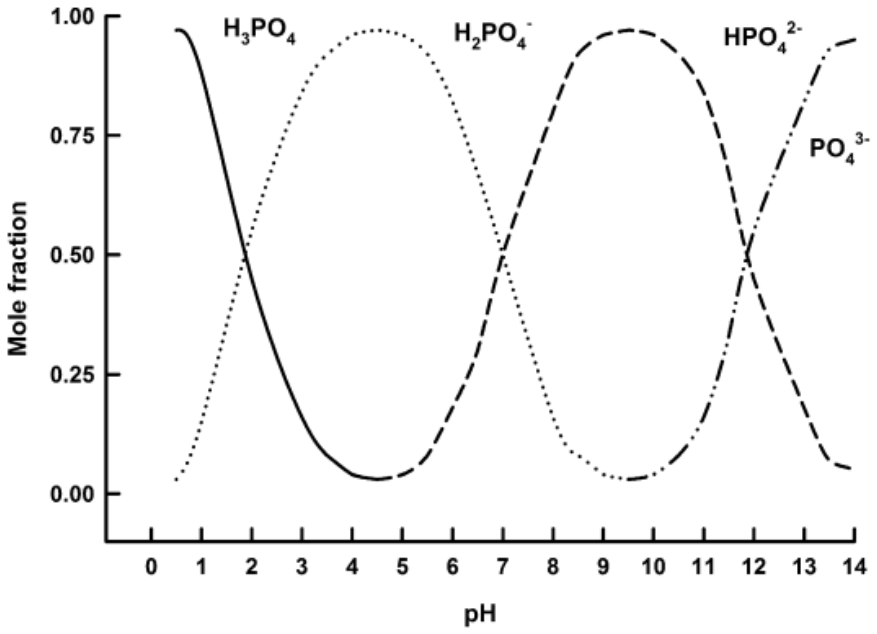

Figure 1: Effects of pH on relative proportions (mole fractions) of H_3PO_4, $H_2PO_4^-$(di-orthophosphate), HPO_4^{2-}(mono-orthophosphate ions), and PO_4^{3-} in an orthophosphate solution (Boyd, 2015)

2.3 Technologies for the Removal of Phosphate from Wastewater

Development of technologies for phosphate removal started in the 1950s in response to the issue of eutrophication and the need to reduce the levels of phosphate entering surface waters. Several physicochemical and biological processes have been investigated for removing dissolved phosphate in water and wastewaters. To ensure reliable low phosphorus concentration in the effluent from wastewater treatment plant it is necessary to combine treatment technologies and apply three-stage process. Usually these stages are physical, biological and chemical.

2.3.1 Physical methods

Phosphorus can be present in water in form of solid material and also in dissolved form. Physical methods used for phosphorus removal include:

2.3.1.1 Gravity Separation/Sedimentation

Gravity separation refers to the removal of suspended solids whose specific gravity difference from that of water causes them to settle or rise during passage through a tank or basin under quiescent conditions. Separation by settling is termed sedimentation; separation by rising is termed flotation. The size of particles determines the fluid drag retarding this separation. For a given specific gravity, smaller particles having greater surface area encounter more drag and hence are more difficult to separate. Tanks or basins, in which sedimentation is carried out, also called clarifiers, may be classified as horizontal flow or vertical flow according to the predominant direction of the flow path from inlet to outlet. It should be noted that, depending on placement of inlets and outlets, certain designs particularly small radial flow tanks may have a flow path with significant components in both horizontal and vertical directions. Settling is a cheap, passive method of phosphorus separation. It requires big areas for sedimentation tanks. It is also called clarification and can be done in units of different construction, such us horizontal clarifier, vertical clarifier, flotation unit and others (Salanko, 2013).

2.3.1.2 Infiltration (Sand Filters)

Filtration is the process by which water flows slowly through a bed of granular media, usually sand, anthracite coal, or granite. As the water passes through the medium, particles become trapped due to several mechanisms: interception, flocculation, straining, and sedimentation. Filters can operate as either slow or rapid sand filters. Slow sand filters conventionally use only sand (with a gravel support layer), but rapid sand filters use a variety of media. Single-medium beds use only sand, but dual-media filters use sand and anthracite coal. Mixed-media beds use coal, sand, and garnet (Mackenzie L. Davis, 2014). Filtration is a method where filtrating material is used. During the filtration process more than 80% of particulate is captured, while less than 2% of dissolved material removed. Share of soluble phosphorus for municipal wastewater is about 90%. This means that conventional sand filters will not provide required water quality regarding phosphorus content and must be applied together with other treatment methods which is shown in figure 2. Disadvantages of filtration is that it removes only particulate and require large area required to build the filter (Stepan, 2015).

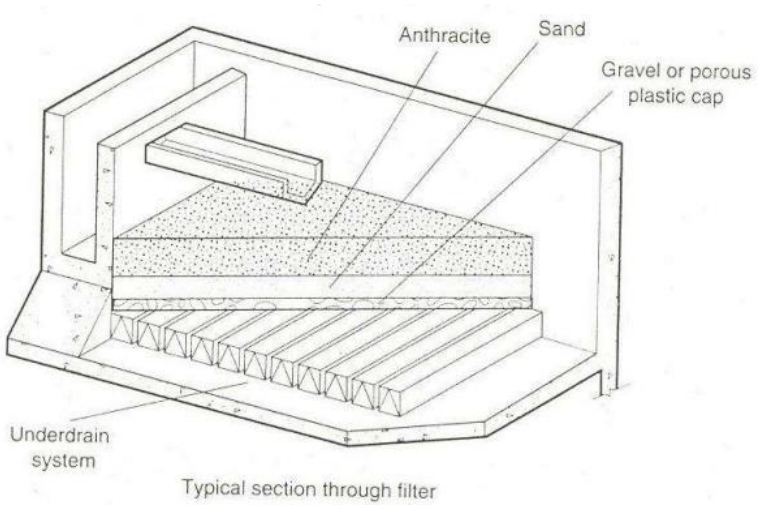

Figure 2: Conventional sand filters

2.3.1 Chemical methods

Chemical phosphorus removal is achieved by adding metals ions that are able to form precipitates with inorganic phosphates that are dissolved in the water. The wastewater phosphorus is bound with coagulants containing two or three valent metal salt such as iron and aluminum chloride or sulfate, or calcium hydroxide. The coagulants react with phosphorus and other impurities in wastewater (Ashok Bankar, 2018).

The effectiveness of a chemical precipitation process is dependent on several factors, including the type and concentration of ionic metals present in solution, the precipitant used, the reaction conditions (especially the pH of the solution), and the presence of other constituents that may inhibit the precipitation reaction (YaserDahman, 2017).

During chemical purification of wastewater, the reagent ions interact with soluble salts of the orthophosphoric acid, thus creating highly dispersed colloid phosphate sediment. Meanwhile, the chemical reacts with water-borne bases to produce large-flake sediment. This sediment triggers coagulation of the high-dispersion colloid phosphate sediment and suspension, it also adsorbs some of the phosphorus-bearing organic compounds, and then it is withdrawn from the system. Salts of two- and three-valent metals are used as reagents. The practice of wastewater treatment widely uses such coagulants as aluminum and iron salts, and also lime (Olga Ruzhitskaya, 2017).

Aluminum sulfate can be purchased as either dry or liquid alum $Al_2(SO_4)_3.14H_2O$ Commercial alum has an average molecular weight of 594, with approximately 14 waters of hydration. Alum reacts with alkalinity according to the following reaction (Mackenzie L. Davis, 2014):

$$Al_2(SO_4)_3.14H_2O + 6HCO^-_3 \rightleftharpoons 2Al(OH)_3(s) + 6CO_2 + 14H_2O + 3SO_4^{2-} \quad \text{..... (4)}$$

Such that each mole of alum added uses six moles of alkalinity and produces six moles of carbon dioxide. The preceding reaction shifts the carbonate equilibrium and decreases the pH. However, as long as sufficient alkalinity is present and CO_2 (g) is allowed to evolve; the pH will not be drastically reduced. When sufficient alkalinity is not present to neutralize the sulfuric acid production, the pH may be lowered significantly due to the formation of sulfuric acid.

$$Al_2(SO_4)_3.14H_2O \rightleftharpoons 2Al(OH)_3(s) + 3H_2SO_4 + 8H_2O \quad \text{..... (5)}$$

If pH control is a problem, lime or sodium carbonate may be added to neutralize the acid, hereby stabilizing the pH. Two important factors in coagulant addition are pH and dose. The optimum dose and pH must be determined from laboratory jar tests. The optimal pH range for alum is approximately 5.5–6.5, with adequate coagulation possible at pH between 5 and 8 under some conditions. Further on, the following reaction occurs in the presence of phosphates (Mackenzie L. Davis, 2014)

$$Al_2(SO_4)_3.14H_2O + 2PO_4^{3-} \rightleftharpoons 2AlPO4\downarrow (s) + 3SO_4^{2-} + 14H_2O \quad \text{..... (6)}$$

When salts of three-valent iron are used as coagulant, the following reaction occurs:

$$Fe(OH)_3(s) \rightleftharpoons Fe^{3+} + 3OH^- \quad \text{..... (7)}$$

$$Fe_mPO4(OH)_{3m-3}(s) \rightleftharpoons mFe^{3+} + PO4^{3-} + (3-m)OH^- \quad \text{..... (8)}$$

Another iron salt widely used for precipitation of phosphorus is a ferrous sulfate $FeSO_4.7H_2O$, usually known as copperas. It is a cheap byproduct in the steel industry which can be successfully applied in simultaneous precipitation processes (Mbaeze MC, 2017).

Lime addition removes calcium ions as well as phosphorus from wastewater, along with any suspended solids. The lime Ca $(OH)_2$ reacts first with the natural alkalinity in the wastewater to produce calcium carbonate which is primarily responsible for enhancing suspended solids removal: (Gray, 2010)

$$Ca(HCO_3)_2 + Ca(OH)_2 \rightarrow 2CaCO_3 \downarrow + 2H_2O \quad \text{..... (9)}$$

After the alkalinity is removed calcium ions combine with the orthophosphate present under alkaline conditions (pH = 10.5) to form insoluble and gelatinous calcium hydroxyapatite (Ca_5 (OH) $(PO4)_3$):

$$Ca^{2+} + 4\,OH^- + 3HPO_4^{2-} \rightarrow Ca_5(OH)(PO_4)_3 \downarrow + 3H_2\,O \quad \text{..... (10)}$$

There may be certain disadvantages associated with chemical precipitation and simultaneous precipitation in particular. The major drawback of the chemical precipitation is that during phosphorus removal an additional amount of sludge is produced. Situation is becoming worse if lime is used for the primary treatment. Depending on the volume of water necessary for treatment, the cost of this technology can be high. Metal hydroxide sludge typically contains water bound in the chemical matrix and results in a large volume of waste requiring disposal Generation of large volumes of sludge may be problematic if there is not room available. Increased costs from energy use occur when attempting to drive off excess moisture (Grégorio Crini, 2019).

2.3.2 Enhanced biological phosphorus removal method

In respect to recovery of phosphorus, EBPR is a much more favorable technology than chemical phosphorus removal. The phosphorus is taken up in the activated sludge and it is relatively easy to recover the phosphorus compared to chemical sludge. However, the EBPR process is very dependent on the wastewater characteristics and is less stable and flexible compared to chemical precipitation. It normally involves more complex control and larger reactor volumes as well. Normally, under favorable conditions, around 90% of the incoming phosphorus can be contained in the sludge (Metcalf & Eddy, 2014).

Biological phosphorus removal primarily occurs via the accumulation of phosphorus by microorganisms beyond “normal” requirements for metabolic processes (termed luxury uptake). Phosphorus accumulation is as polyphosphate and is retained as an energy reserve for maintenance or to provide a competitive advantage over ordinary heterotrophs (Joshua T. Bunce, 2018). The workhorses responsible of EBPR systems are called polyphosphate accumulating organisms. There exist various types of organisms that are able to take up phosphorus in excess amounts as energy-rich polyphosphates, and the phosphorus content can reach up to 20-30% of the dry weight of the bacteria. For common heterotrophic bacteria the phosphorus content can be about 2%. So the basis of EBPR is to maximize the fraction of PAOs in the wastewater to ensure optimal phosphorus removal (Ivar, 2013).

To stimulate the growth of PAOs, two conditions have to be satisfied:

1. Alternating anaerobic and aerobic conditions (Can be achieved with an anaerobic reactor followed by an aerobic reactor, or with a sequential batch reactor).

2. Sufficient supply of volatile fatty acids (acetate, propionate, etc.) in the anaerobic reactor (Can be supplied by fermentative bacteria in the anaerobic reactor or have a separate tank where fermentation is occurring).

The stored polyphosphates are considered as a phosphate and energy reserves for the PAOs, and this helps PAOs get an advantage over other bacteria in alternating anaerobic and aerobic conditions. The general biochemical transformations in the metabolism of PAOs have been widely accepted in the literature and in textbooks. Different biochemistry models have been proposed in order to understand the metabolism of PAO. The Mino model is the generally accepted model and will be presented Figure 3 (Ivar, 2013).

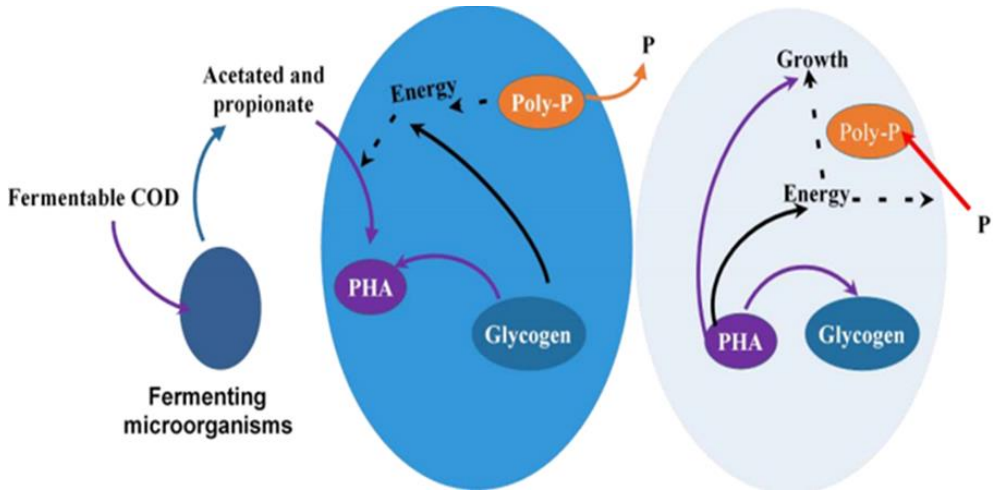

Figure 3: Simplified biochemical model for PAO metabolism: left, anaerobic phase; right, aerobic phase.

In an anaerobic zone In an EBPR system the incoming wastewater is mixed together with the activated sludge. Here PAOs are able to use volatile fatty acids (VFA), such as acetate or propionate, to form poly-hydroxyalkanoates (PHA), which is a carbon storage product (Joshua T. Bunce, 2018).

The volatile fatty acids are already present in the influent or produced by fermentative bacteria present in the anaerobic tank. Fermentation is microbial degradation of organic compounds which occurs in the absence of oxygen and nitrate. So it is essential for the process that the anaerobic tank is free of any oxygen or nitrates, as this may interfere with the fermentation. It is also possible to use a separate tank dedicated to fermentation. To be able to form the PHAs, the PAOs use the stored poly-Phosphaate and glycogen as an energy source (Metcalf & Eddy, 2014).

In the following aerobic or anoxic zone, either nitrate or oxygen is supplied. The PAOs are regenerating their poly-P reserves and are able to take up sufficient orthophosphate so that there is a net removal of phosphorus from the influent. To provide energy for the formation of the poly-P reserves, the PHAs formed in the anaerobic tank are oxidized by oxygen. The energy released is also used for replenishment of glycogen reserves and for growth (Ivar, 2013).

2.4 Iron oxide nanoparticles

Iron oxides have been extensively studied in diverse fields. Recently, functionalized iron oxide nanoparticles have also been used in many advanced nano technological applications. The most important advantage of nano sized iron oxides among other nanomaterials are due to its relatively low toxicity and biodegradability. It is observed that generally, metal oxides show great industrial potential in many advanced applications such as solar energy transformation, electronics, electrochemistry, manufacture of magnetic storage media, sorption and purification processes and catalysis In above all, the applications, iron (III) oxide plays a vital role, especially because of its superior catalytic activity, super paramagnetic behavior, and the large specific surface area of the nanoparticle (Mahapatra, 2015).

Iron oxides are one of the most important metal oxides of technological importance. It has fourteen pure phases i.e., oxides, hydroxides or oxy-hydoxides, which are known till date. These are Fe (OH) $_3$, Fe (OH) $_2$, $Fe_5HO_8 \cdot 4H_2O$, Fe_3O_4, FeO, five polymorphs of FeOOH and four of Fe_2O_3. Characteristics of these oxide compounds include mostly the trivalent state of the iron, low solubility and brilliant colors. Among them mostly are crystalline except few. Further, the oxy hydroxide compounds like goethite, α-FeO (OH) exhibits an orthorhombic symmetry. Similarly, akaganeite, β- FeOOH, has a large tunnel type structure where iron atoms are strongly bonded to the framework. Lepidocrocite, γ- FeOOH, crystal structure is built by double layers of Fe-octahedral, with the hydroxyl groups being located on their external surfaces and hydrogen bonding between the layers. The basic morphology of lepidocrocite are lath-like or tabular (Boris I. Kharisov, 2012).

2.4.1 Fe_3O_4 Nanoparticles

Magnetite is a common magnetic iron oxide that has a cubic inverse spinel structure with oxygen forming a face-centered cubic (fcc) structure and Fe cations occupying interstitial tetrahedral sites and octahedral sites. The electrons can hop between Fe^{2+} and Fe^{3+} ions in the octahedral sites at room temperature, thus giving the magnetite properties of half-metallic material. Using chemical precipitation methods, different nanometer-scale MFe_2O_4 materials (M = Fe, Co, Ni, Mn, Mg, etc) can be synthesized and used in studies of nanomagnetism (Daoush, 2017).

Fe_3O_4 nanoparticles have attracted considerable interest due to their superparamagnetic properties and their potential biomedical applications arising from its biocompatibility and non-toxicity. Among other industries, Iron oxide Fe_3O_4 nanoparticles are used as magnetic data storage, biosensors, drug-delivery, ferrofluids, magnetic coatings, EM-waves absorbing coatings, wastewater purification. During magnetic separation, for example, the application of a magnetic field enables to selectively collect a magnetic responsive material such as magnetic iron oxide (Fe_3O_4) nanoparticles. This technology is applied to water treatment such as removal of heavy metal ions, pesticide, toxic water soluble molecules, and oily water treatment. In addition to the applications already mentioned, iron oxide nanoparticles play crucial rules in dozens of other magnetic devices and applications, such as medical imaging, cell separation, and refrigeration (Attarad Ali, 2016).

2.4.2 Properties of Magnetite (Fe_3O_4) Nanoparticles

Physical Properties

Natural and synthesized magnetite micro-scale crystals exhibit metallic luster and opaque jet black color. Magnetite's density is established at 5.18 g/cm^3, slightly lighter than reddish-brown hematite (α-Fe_2O_3; 5.26 g/cm^3) and somewhat heavier than yellowish-orange ferrihydrite (α-FeOOH; 4.26 g/cm^3); pure iron (α-Fe) has a density of 7.87 g/cm^3. At ambient temperatures, magnetite particles exhibit hardness of 5.5, identical to glass. Effective surface areas of magnetite vary according to synthesis method as certain procedures generate coarser/finer particles; however, typical micro-scale particles with approximate diameters of 0.2 µm exhibit surface areas of approximately 6 m^2g^{-1} (K. Sairam Goud, 2017).

Standard Gibb's free energy of magnetite formation is - 1012.6 kJ/mol; therefore, formation of magnetite is thermodynamically favorable. Additionally, the standard enthalpy and entropy of magnetite formation are -1115.7 kJ/mol and 146.1 kJ/ K.mol, respectively. Solubility products differ depending on the applicable dissolution reaction; however, generally speaking magnetite dissolution is much faster than other pure ferric oxides (Blaney, 2007).

Structural Properties

Magnetite and maghemite form a close-packed cubic lattice with the iron ions located at interstices between the oxygen ions. These materials have a spinel crystal structure. There are two different interstices that the metal ions can occupy: tetrahedral sites and octahedral sites as shown in figure 4. In the cubic structure of both iron oxides, one-third of interstices are coordinated with oxygen ions in a tetrahedral structure, while two-thirds are bonded in octahedral sites. The key difference between Fe_3O_4 and γ-Fe_2O_3 is that in the case of Fe_3O_4, Fe^{2+} is in eight tetrahedral sites, while Fe^{3+} ions occupy 16 octahedral sites in a unit cell. In the case of γ-Fe_2O_3, tetrahedral and octahedral sites are occupied by Fe^{3+}.Magnetite contains both Fe^{2+} and Fe^{3+} within a stoichiometry Fe^{2+}/Fe^{3+} of 0.5. Nevertheless, magnetite is often nonstoichiometric, resulting in a cation-deficient Fe (III) layer. The crystal forms of magnetite include octahedron and rhombodecahedron and the specific surface area ranges from 4 to 100 m^2/g. The crystal structure of magnetite is inverse spinel with a unit cell consisting of 32 oxygen ions in a face-centered cubic structure and a cell parameter of 0.839 nm. At temperatures above 120K, Fe^{2+} and half of the Fe^{3+} occupy octahedral sites and the other half of the Fe^{3+} occupies tetrahedral sites (Haddad, 2017).

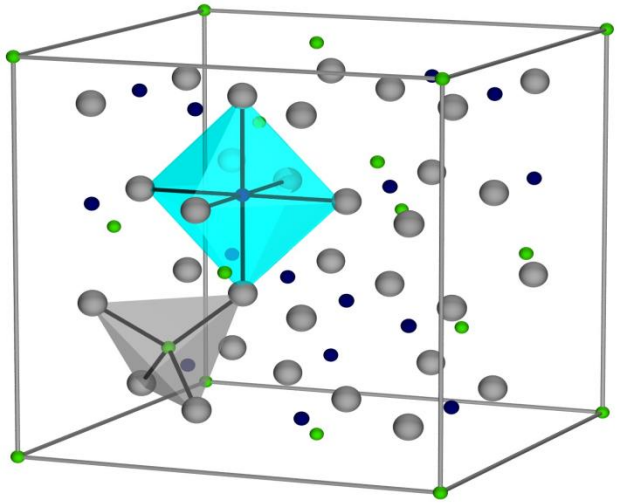

Figure 4: The iron sites with tetrahedral (in the spinel structure) or prismatic oxygen coordination and iron sites with the octahedral oxygen coordination (Haddad, 2017).

Thermal property

Magnetite comes from the Spinel mineral family. It mostly possesses different kinetic-based characteristics: the behaviour of MNPs differ at three different phases of temperature. The first phase is the Verwey temperature, where the Verwey transition ranges between 0 K and 119 K. At this phase, magnetite converts from semiconductor to metal phase. The second phase is the Curie temperature (*TC*), ranging between 120 K and 840 K. The third phase is when the temperature is above 840 K, where MNPs behave as a paramagnetic metal In terms of electrical conductivity, a significant decline in temperature at around 120 K of the order of 90 times caused the MNPs to convert from cubic structure to orthorhombic structure, which is a lower ordering of symmetry . The thermal properties of MNPs are highly important in the biomedical field, especially for the usage of MNPs as thermal seeds in magnetic hyperthermia therapy MHT (Lokesh Srinath Ganapathe, 2019).

Magnetic Properties

Magnetite's Curie temperature is observed at 850 K. below the Curie temperature, magnetic moments on tetrahedral sites, occupied by ferric species, are ferromagnetically aligned while magnetic moments on octahedral sites, occupied by ferrous and ferric species, are antiferromagnetic and cancel each other; such combined behavior is termed ferrimagnetic as shown in table 1. Therefore, at room temperature, magnetite is ferromagnetic. As temperatures increase to the Curie temperature, thermal fluctuations destroy the ferromagnetic alignment of magnetic moments on tetrahedral sites; hence, ferromagnetic strength is diminished. When the Curie temperature is attained, net magnetization becomes zero and superparamagnetic behavior is observed (Lee, 2007).

Table 1: Spin magnetic moment distribution of Fe^{3+} and Fe^{2+} ions in Fe_3O_4 elemental cell

Cation	Octahedral Site	Tetrahedral Site	Net Magnetic Moment
Ferric ions	↑↑↑↑ ↑↑↑↑	↓↓↓↓ ↓↓↓↓	Complete annihilation
Ferrous ions	↑↑↑↑ ↑↑↑↑	-	↑↑↑↑

As particle size is decreased, the amount of exchange-coupled spins resisting spontaneous magnetic reorientation is decreased, tending towards paramagnetic or superparamagnetic magnetization. Consequentially, decreasing magnetite particle size should demonstrate reduced ferrimagnetic and enhanced superparamagnetic behavior (Lokesh Srinath Ganapathe, 2019).

Chemical Properties

The reduction in particle size Fe_3O_4 nanoparticles affects the interaction of particle in chemical reactions. When size of the particle decreases, more number of dangling bonds are exposed to the environment involving in the chemical reactions/processes. It has been observed that if size of the particle is decreased, then the reaction speed increases exponentially. The additional benefit obtained from nanosize of the particle is the reduction in the temperature of reaction flow. Also at nanoscale, few reactions are possible that do not happen in bulk size (Bauer, 2020).

2.4.3 Synthesis of Fe_3O_4 Nanoparticles

The manufacture of nanoparticles can be broadly defined into two approaches. The first is the top down approach and involves a material undergoing significant size reduction via physical or chemical processes. During size reduction, the resulting particle size, shape, and surface structure are heavily dependent on the technique used. Unfortunately, size reduction also tends to introduce surface imperfections that can significantly impact the overall physicochemical properties of the fabricated nanoparticle. The second, bottom up approach builds nanoparticles via the assembly of atoms, molecules, and smaller particles or monomers (Derek Fawcett, 2017). There are three main routes for the synthesis of Fe_3O_4: chemical, physical and biological. These have been investigated in order to produce more stable, soluble, biocompatible, and shape and size-controlled nanoparticles (Ali, 2016).

2.5.2.1 Green (Biological) method of Fe_3O_4 nanoparticles synthesis

Generally, green synthesis of Fe_3O_4 nanoparticles means the synthesizing of nanomaterial's or nanoparticles without using hazardous chemicals that produce toxic byproducts. In other words, green method is an eco-friendly technique to synthesize nanoparticles where it is not harmful to the environment and human health. The biological compounds present in green materials may act as both reducing and capping agents that can stabilize the nanoparticles during the synthesis process. This can control the size and shape of the nanoparticles which can be used in various applications (Jayanta Kumar, 2014).

There are a lot of successful studies where Fe_3O_4-NPs can be synthesized using different biological routes, however plant extract is the most extensively used in green synthesis because it can be obtained easily, large-scale production, cost effective and environmental benign. In addition, extracts from plants can act as reducing and stabilizing agents in the nanoparticles synthesis which might be due to the presence of phytochemicals. Phytochemicals are compounds that are produced by plant itself (Yen Pin Yew, 2018).

2.5.2.2 Physical method of Fe_3O_4 nanoparticles synthesis

Most important physical approaches include evaporation-condensation and laser ablation. Various metal nanoparticles such as silver, gold, lead sulfide, cadmium sulfide, and fullerene have previously been synthesized using the evaporation-condensation method. The absence of solvent contamination in the prepared thin films and the uniformity of nanoparticles distribution are the advantages of physical approaches in comparison with chemical processes. The absence of solvent contamination in the prepared thin films and the uniformity of nanoparticles distribution are the advantages of physical approaches in comparison with chemical processes (Iravani, 2012). The disadvantages of physical methods are high radiation and highly concentrated reductants and stabilizing agents that are harmful for the environmental and to human health (Khadeeja Parveen, 2016).

2.5.2.3 Chemical method of Fe_3O_4 nanoparticles synthesis

These methods are simple, tractable, and efficient, in which the size, composition, and even the shape of the NPs can be managed. Iron oxides can be synthesized through the coprecipitation of Fe^{2+} and Fe^{3+} by the addition of a base. The size, shape, and composition of iron NPs synthesized through chemical methods depend on the type of salt used, Fe^{2+} and Fe^{3+} ratio, pH, and ionic strength. In the last decades, much research has been developed to the synthesis of iron oxide NPs, and many reports have described efficient synthesis approaches to produce the shape-controlled, stable, biocompatible, and monodispersed iron oxide NPs (Walid, 2017).

The most common methods including co-precipitation, thermal decomposition, hydrothermal synthesis, microemulsion, sonochemical synthesis, and sonochemical synthetic route can all be directed to the synthesis of high quality of iron oxide NPs (Wei Wu, 2008). In this study Coprecipitation technique was used to synthesize Fe_3O_4 nanoparticles Coprecipitation is an easy and economical way to synthesize iron oxides nanoparticles (Fe_3O_4, γ-Fe_2O_3) or ferrites of transition metals From aqueous M^{2+}/Fe^{3+} salt solutions ($M^{2+} = Fe^{2+}, Co^{2+}, Ni^{2+}, Zn^{2+}, Mn^{2+}$) added to a base ($NH_4OH$,NaOH, Na_2CO_3) under atmosphere condition At either room temperature or elevated temperatures. The size distribution, shape, and composition of magnetic nanoparticles depends on the pH value, temperature, M^{2+}/Fe^{3+} ratio, ionic strength, as well as the presence of oxidant species (M. Padervanda, 2014).

2.5 Application Iron Oxide Nanomaterial in Wastewater Treatment

Presently, nanotechnology is assumed relatively better and superior to prepare nano adsorbent/materials of desired quality and characteristics to remove these toxic pollutants from wastewater. Their small size provides them with appropriate dispersibility, high surface area, porosity, and tunable reactivity. They can be dispersed appropriately. Under the right formulation and in the presence of stabilizing agents, nanoparticles can travel just like water in soil, and when in the liquid phase, they quickly scrutinize large volumes. Likely, their reactivity can be tuned to be enough to attack organic and inorganic molecules, but not enough to attack life forms (Ravindra Kumar Gautam, 2016).

MNMs are normally composed of magnetic elements, i.e., iron, nickel, cobalt, or their oxides like maghemite (Fe_2O_3), magnetite (Fe_3O_4), cobalt ferrite ($CoFe_2O_4$), nickel ferrite ($NiFe_2O_4$), etc. Normally, MNMs are capped with organic layers (polymers or surfactants such as polyethylene glycol and dextran) or inorganic elements (gold, platinum, cobalt oxide, aluminum oxide silica, activated carbon, etc.) in order to make them stable against aggregation, oxidation, and corrosion. That's the reason; presently nanotechnology is assumed as an emerging and innovative technology also for biomedical and environmental applications (Imran Ali, 2019).

2.5.1 Adsorption Mechanism of phosphorus using magnetite

Adsorption is a surface phenomenon with common mechanism for organic and inorganic pollutants removal. When a solution containing absorbable solute comes into contact with a solid with a highly porous surface structure, liquid–solid intermolecular forces of attraction cause some of the solute molecules from the solution to be concentrated or deposited at the solid surface. The solute retained (on the solid surface) in adsorption processes is called adsorbate, whereas, the solid on which it is retained is called as an adsorbent. This surface accumulation of adsorbate on adsorbent is called adsorption (Rashed, 2013).

Specifically, the adsorption-based process is considered a superior technique in terms of cost, flexibility, and simplicity of design/operation and insensitivity to toxic pollutants, producing a high-quality effluent without the additional formation of any harmful substances Apart from the efficiency for removal of contaminants, the main target of adsorption-based nanotechnology is the development of low-cost and environmentally friendly adsorbent nanomaterials able to be regenerated and reused (Dimitris Dermatas, 2018).

The adsorption mechanism of pollutants onto iron oxide surfaces is debatable. Some researchers have showed that the process is based on van der Waals interactions (physisorption) with the oxide surface, some have reported chemical reactions with the functional groups (chemisorption), and others reported ion exchange of pollutant ions in aqueous solution with iron ions in the iron oxide lattice structure (B. Xing, 2005).

The apparent contradictions in the literature findings could, nevertheless, be explained when all factors contributing to pollutant removal are analyzed in light of the controlling mechanisms. Nonetheless, generally in an aqueous solution the surface of iron oxide/hydroxide nanoadsorbents may undergo protonation/deprotonation as per the following reaction (B. Xing, 2005):

$$H_2O + Fe\,O^- \overset{H^+}{\rightleftharpoons} Fe\,OH \overset{H^+}{\rightleftharpoons} Fe\,OH_2 \quad \text{..... (11)}$$

$$\overset{OH^-}{} \qquad \overset{OH^-}{}$$

Where H^+ and OH^- refer to the potential determining ions. This feature allows the iron oxide nanoadsorbents to be suitable for removal of different types of contaminants such as anions, cations, and organic based pollutants. In addition, this surface property provides the potential for nanoadsorbent regeneration. Depending on the phase of iron oxide/hydroxide and their surface properties such as pHpzc, their highest adsorption capacity can be at low pH or high pH region. For instance, depending on the pH of solution, metal ions can present as stable ions or hydrolyze to form a series of mononuclear and polynuclear hydroxy as per the following general reaction (Mengxue Li J. L., 2016).

$$xM^{n+} + yH_2O \rightleftharpoons M_x(OH)_y^{n-y} + yH^+ \quad \text{..... (13)}$$

In most metal ions the dominant species is $M(OH)_2$ at pH > 6.5 and M^{2+} and $M(OH)^+$ at pH < 6.5. Thus, ion adsorption on iron oxide surfaces is likely to be electrostatic attraction. In a relatively basic solution, a significantly high electrostatic attraction exists between the negatively charged surface of iron oxide and the metal ions. As the pH of the solution decreases, the number of positively charged sites increases and the number of negatively charged sites decreases. This would allow iron oxide nanoadsorbents to treat much higher amount of wastewater without the need for pH adjustment (Bhatnagar, 2012).

Bulk Fe_3O_4 is an ubiquitous magnetic iron oxide that occurs in the lithosphere, pedosphere, and biosphere and usually contains both ferrous and ferric (Fe (II) and Fe (III)) iron species; its general type is $Fe(II)Fe(III)_2O_4$. The crystal structure of Fe_3O_4 follows an inverse spinel structure where octahedral and tetrahedral/octahedral layers are being alternated. Fe_3O_4

nanoparticles exhibit amphoteric surface activity, high dispersibility, and high metal adsorption capacity, and they can be easily separated by using an external magnetic field, making their regeneration and subsequent reuse much easier (Ekain Cagigal, 2018).

Fe_3O_4 has been extensively studied as a heavy metal adsorbent for both oxyanionic and cationic forms. Cr and As are common metals widely found in groundwater due to geogenic contamination, resulting from the oxidation of naturally occurring Cr(III) in certain geologic formations such as ultramafic rocks, and due to its release through rock weathering and volcanism, respectively. In the geoenvironment, Cr occurs either in its highly soluble hexavalent (Cr (VI)) or in the insoluble trivalent (Cr (III)) form. X-ray photoelectron spectroscopy (XPS) and X-ray absorption near edge structure (XANES) analysis have shown that Cr(VI) adsorption is a strongly pH-dependent process with adsorption capacity being maximized at pH values lower than the point of zero charge (PZC) of Fe_3O_4 (pH_{PZC} = 6.5). Cr (VI) adsorption is based on electrostatic attractions between the Cr (VI) anions (chromates) and the positively charged surface (Ekain Cagigal, 2018).

Particles of magnetite are also used for phosphorus removal as an additional to coagulants agent to facilitate separation of solid and liquid phases. This method could also be used for other non-magnetic substances like suspended solids, organic substances, algae and viruses. In case of phosphorus removal the ordinary coagulants for chemical precipitation are used with subsequent or simultaneous adding of magnetite. This method has improvement compared to common precipitation: less time needed for coagulant settlement, better extraction of settled particles and therefore smaller volume of tanks needed (Ahmad Abo Markeb, 2016).

Magnetite for wastewater treatment has several advantages. Of course, its main advantage is possibility of using magnetic field in order to separate magnetite from the water. This results in shorter sedimentation time, and thus, in size reduction and space saving. There is no sludge production during magnetite usage for wastewater purification, it could be easily renovated and recycled back into the process. The other positive thing is that magnetite can be synthesized directly at the WWT facility, so no additional transportation is needed (M. Ruthiraan, 2019).

2.6 Factor affecting Adsorption Process

2.6.1 Effect of solution pH on phosphate adsorption

The pH of the phosphate solution plays an important role in the whole adsorption process and particularly on the adsorption capacity. It has been reported that the solution pH can alter the adsorption/desorption of phosphate to/from iron oxide-based materials by changing the amount of charge and the charge characteristics of the phosphate and the surface of the materials and further changing the dominant adsorption/desorption mechanisms (Lei Hou Q. L., 2020).

Thermodynamic calculations have revealed that phosphate in aqueous solution exists as $H_2PO_4^-$, HPO_4^{2-} and PO_4^{3-} at different ratios depending on the solution pH, with pK_1=2.15, pK_2=7.20 and pK_3=12.33, respectively. The adsorption ability of the surface and the type of active centres on the surface are indicated by a significant factor called the point of zero charge (pH_{pzc}). When pH > pH_{pzc}, the phosphate adsorption may be affected by the electrostatic repulsion and increasing competitive effect of OH^- ions for the active sites on the sorbent. When pH < pH_{pzc}, the sorbent surface is positively charged, favoring adsorption of the anions (Mengxue Li J. L., 2016).

2.6.2 Effect of Adsorbent dosage on phosphate adsorption

The optimum adsorbent dosage is a key parameter, which affects the amount of adsorbed adsorbate. The surface area increases with increasing adsorbent dosage. In order to avoid consuming an excess amount of adsorbent, the finding an optimal dosage is necessary. Several research groups have investigated the influence of adsorbent dosage by varying the adsorbent dosage concentration (Malihe Pooresmaeil, 2020).

Commonly, the removal efficiency increases by increasing the amount of adsorbent dosage, due to the increasing number of accessible active sites of adsorbent. However, after a certain adsorbent dosage, the adsorption capacity remains constant. This constant is generally due to the presence of a large number of accessible surface-active groups compared to the adsorbate amount (Namazi, 2020).

2.6.3 Effect of contact time on phosphate adsorption

The contact time significantly affects the adsorption process. Also, contact time can influence the economic efficiency of the process as well as the adsorption kinetics. Therefore, contact time is another performance governing factor in adsorption process (Sidra Iftekhar, 2018). Previous study shows that the adsorption process commonly occurs in three stages: first, rapid adsorption occurs, subsequent adsorption becomes slow, and finally, adsorption reaches the equilibrium state and remains constant. The high adsorption capacity in the first step could be related to the rapid attachment of adsorbate molecules to the surface adsorbent through surface mass transfer. The second step is slower and probably related to occupying the available external sites in the first step. Finally, the accessible adsorption sites become rarer in the third step, causing the equilibrium state (Namazi, 2020).

2.6.4 Effect of initial concentration of phosphate on adsorption

The initial concentration of the phosphate in the solution can alter the pollutant removal efficiency of an adsorbent that relies on the combination of pollutant concentration and available binding sites on the surface of the adsorbent. The initial pollutant concentration can provide the required driving force to repress the mass transfer resistance of pollutant between the solid (adsorbent) and liquid (contaminated water) phases (Sinha Ray, 2020).

2.7 Adsorption isotherm study

Adsorption process is a surface phenomenon in which adsorbates transfer onto adsorbents. Over the past decades, adsorption technology has been widely applied for the water and wastewater treatment because it is low-cost, efficient, simple, and environmentally friendly. Modeling of adsorption data by isotherm models is the most convenient and widely used one. In addition, the adsorption isotherm models can provide information of the maximum adsorption capacity, which is significant in the evaluation of the performance of the adsorbents.

2.7.1 Langmuir isotherm model

According to Langmuir theory, adsorption process onto a solid surface is based on a kinetic principle in which continuous bombardment processes of molecules onto the surface with corresponding molecules' desorption or evaporation from the surface with zero accumulation rates at the surface. In other words, rates of adsorption and desorption should be equal. Traditionally, the Langmuir isotherm model has been utilized for quantifying and contrasting adsorption capacity of various bio-sorbents (Mohammad A. Al-Ghouti, 2020). For sorption of solutes from aqueous solution, the basic isotherm is expressed as

$$q_e = \frac{q_{max} K_L C_e}{1 + K_L C_e} \quad \ldots\ldots\ldots\ldots\ldots (14)$$

q_e is amount of sorbate sorbed per mass of sorbent (mg/g), C_e is the equilibrium sorbate concentration in molar or mass units (residual P concentration in a solution in mg P/l), X_{max} is the maximum sorption capacity (mg P/g), and K_L is a binding constant related to the energy of sorption (L/ mg) A plot of X versus C is a hyperbola. The isotherm can be rearranged in the form of (y=b + ax) as $\frac{1}{q_e} = \frac{1}{q_m} + \frac{1}{K_L q_{max}} . \frac{1}{C_e}$ from the graph of $\frac{1}{q_e}$ v_s $\frac{1}{C_e}$ we can get the value of X_{max}(the maximum sorption capacity) and K_L.

To find out the probability of isotherm, the important characteristics of Langmuir isotherm can be expressed interms of a dimensionless constant separation factor or equilibrium parameter, R_L

$$R_L = 1 / (1 + K_L C_0) \quad \ldots\ldots\ldots\ldots\ldots (15)$$

Where K_L is the Langmuir isotherm constant and C_0 is the initial concentration of phosphate (mg L^{-1}). The values of $K_L > 1$, $K_L = 1$, and $K_L < 1$ reflect that the adsorption is unfavorable, linear, and favorable, respectively (Jianlong Wang, 2020).

2.7.2 Freundlich isotherm

The Freundlich model is an empirical equation based on adsorption on a heterogeneous surface.The Freundlich model is expressed by the equation:

$$q_e = K_F C_e^{\,1/n} \quad \ldots\ldots\ldots\ldots\ldots (16)$$

$$\ln q_e = \ln K_f + \frac{1}{n}\ln C \text{ ..... (17)}$$

Where X = amount of sorbate sorbed per mass of sorbent (e.g., g/g), C = is the equilibrium sorbate concentration in molar or mass units (residual P concentration in a solution in mg P/l) K_F and $\frac{1}{n}$ are constants related to the adsorption capacity and affinity, respectively. When 1/n is greater than zero (0 < 1/n < 1) the adsorption is favorable, when 1/n is greater than 1, the adsorption process is unfavorable, and it is irreversible when 1/n = 1. (Augustine Amalraj, 2017).

2.8 Adsorption Kinetics study

Adsorption kinetics is a curve (or line) that describes the rate of retention or release of a solute from an aqueous environment to solid-phase interface at a given adsorbents dose, temperature, flow rate and pH (George William Kajjumba, 2018).

2.8.1 Pseudo first order model

The pseudo-first-order (PSO) kinetic model explains the relationship between the rate the sorption sites of the adsorbents are occupied and the number of unoccupied sites. It is defined using the Lagergren equation as follows (Ifelebuegu, 2020):

$$\frac{dq_t}{dt} = k_1 (q_e - q_t) \text{..... (18)}$$

Where, q_e = amount of adsorbate adsorbed at equilibrium (mg/g); q_t = amount of adsorbate adsorbed at time, t (min) and k_1 = equilibrium rate constant of pseudo first-order adsorption (1/min). After integration with the initial condition $q_t = 0$ to $q_t = q_t$ and t = 0 to t = t; we obtain the linearized form of this equation:

$\ln(q_e - q_t) = lnq_e - k_1 t \leftrightarrow$ y = b-ax which is in linear form..... (19)

Where, values of k_1 can be calculated from the plot of $\ln(q_e - q_t)\ v_s$ t.

2.8.2 Pseudo-second-order modeling

The pseudo-second order (PSO) rate equation is described by the Equation (3), the driving force, (qe - q_t), is proportional to the available fraction of active sites (Keno David Kowanga*, 2016)

$$\frac{dq_t}{dt} = k_2(q_e - q_t)^2 \text{ ..... (20)}$$

Integrating Equation (3) with the boundary conditions of $q_t = 0$ at $t = 0$ and $q_t = q_t$ at $t = t$, yields

$$\frac{1}{q_e - q_t} = \frac{1}{q_e} + k_2 t \text{ ..... (21)}$$

Where k_2 is the second order rate constant. Equation (4) can be rearranged in order to obtain a linear equation:

$$\frac{t}{q_t} = \frac{1}{k_2 q_e^2} + \frac{1}{q_e} t \text{.....(22)}$$

By comparing the correlation coefficient (R^2) of both pseudo first and second order kinetic model we can decide which adsorption model will fit with the adsorption data.

2.9 Common characterization Techniques for Fe_3O_4 nanoparticles

2.9.3 Fourier transforms infrared spectroscopy

FTIR spectroscopy is an absorption/transmission method used to probe chemical bonds and their crowding environment in molecular systems. From the IR spectrum, one can observe the absorption and emission due to the molecular vibration and rotation in the electromagnetic wave infrared region (4000 - 400 cm^{-1}). The IR spectrum reveals the unknown composition qualitatively according to the characteristic frequency of the bands and determines the content of component in a sample (quantification according to band intensity). It can also reveal the molecular structure (such as functional group, bond), identify isomer, and determine structures of compounds (Narendra Kumar, 2016).

This method can be used to measure samples in the gaseous, liquid, and solid states. Modern FTIR instruments are effective at measuring different classes of molecular substances in a short amount of time (Narendra Kumar, 2016).

IR absorption measurement is plotted with wavenumber in cm^{-1} along the *x*-axis and absorption intensity or % transmittance along the *y*-axis. Transmittance, T, is the ratio of the radiant power transmitted by the sample (I) to the radiant power incident on the sample (I_0). Absorbance (A) is given by the equation (András E.Vladára, 2020)

$$A = {}^{\log 1}/_{T} = -\log T = -\log {}^{I}/_{I_0} \quad \ldots\ldots\ldots\ldots\ldots\ldots\ldots\ldots (26)$$

2.9.1 Thermogravimetric analysis

Thermogravimetry is a process of determining material weight with respect to a combination of temperature and time. TGA is a commonly used instrument based on this process to investigate thermal characteristics of a substance under heating environments. The instrument can increase the temperature up to 2000°C and test a specimen weight up to 1 g. TGA uses of a radiant heating chamber, temperature controller, precision balance, gas feeding system, and data analyzer. A piece of specimen (7–8 mg) or powder is placed in a platinum basket and the temperature is continuously recorded by a thermocouple under the basket. Generally, two types of plot are available as results. A plot of specimen weight against temperature (TGA curve) provides thermal decomposition temperatures with residue amount as a function of temperature. The second plot, a derivative of the TGA curve, indicates mass loss rate depending on an increase in temperature (Oisik Das, 2019).

2.9.2 X-ray diffraction

X-ray diffraction is one of the most extensively used techniques for the characterization of NPs. Typically; XRD provides information regarding the crystalline structure, nature of the phase, lattice parameters and crystalline grain size. The latter parameter is estimated by using the Scherrer equation using the broadening of the most intense peak of an XRD measurement for a specific sample. An advantage of the XRD techniques, commonly performed in samples of powder form, usually after drying their corresponding colloidal solutions, is that it results in statistically representative, volume-averaged values. The composition of the particles can

be determined by comparing the position and intensity of the peaks with the reference patterns available from the International Centre for Diffraction Data (ICDD, previously known as Joint Committee on Powder Diffraction Standards, JCPDS) database. However, it is not suitable for amorphous materials and the XRD peaks are too broad for particles with a size below 3 nm (Stefanos Mourdikoudis, 2018).

The XRD spectra that are generated by most software processing the data collected from XRD instrumentation experiments are not in the form of diffraction patterns but in the form of peaks on an x- and y-axis scale. The x-axis is multiples of the diffraction angles 2θ, and the y-axis is the intensity (Narendra Kumar, 2016).

X-ray diffraction is based on constructive interference of monochromatic X-rays and a crystalline sample. The interaction of the incident rays with the sample produces constructive interference when conditions satisfy Bragg's Law

$$n\lambda = 2dsin\theta \quad \ldots\ldots\ldots\ldots\ldots\ldots\ldots\ldots (24)$$

Where d is the spacing between adjacent lattice planes, λ is the wavelength of X-ray radiation, n is an integer (=1) and θ is the diffraction angle or Bragg angle (Igwebike-Ossi, 2017). Broadening of peaks in the X-ray diffraction pattern occurs when the crystallite size of the powder sample reaches below a certain limit (<200 nm). Thus, XRD patterns can be used to estimate the crystallite size of very small particles, using the Scherrer formula

$$d = {k\lambda}/{\beta cos\theta} \quad \ldots\ldots\ldots\ldots\ldots\ldots\ldots\ldots (25)$$

with K the shape factor taken to be 0.94, λ= 1.5416 Å the wavelength isolated from the copper emission as X-ray source, β the full peak width at half the maximum intensity (FWHM) and θ the Bragg angle both in radians, was used (Aidin Lak, 2013).

2.9.4 Scanning Electron Microscope

Scanning electron microscope is one of the most widely used techniques used in characterization of nanomaterials and nanostructures. The signals that derive from electron-sample interactions reveal information about the sample including surface morphology

(texture), chemical composition of the sample. Although the SEM image is a two dimensional (2D) representation of the three-dimensional (3D) objects from a certain viewing angle, the SEM image does contain a certain amount of 3D information that with model-based measurement can be used to reconstruct the shape with sub-nm accuracy of a simple structure (Sagadevan S, 2015)

The signal responsible for the creation of a SEM image is given by the secondary electrons (SEs) and/or backscatter electrons (BSE) created when the sample is bombarded by the primary electron (PE) beam. The typical maximum accelerating voltage of a SEM is 30 kV. Whilst the SE due to their low energy below 50 eV have a small escape depth in the range of a few nm, the BSE possess significantly higher kinetic energies (up to the excitation energy) and come from about a half of the depth of the interaction volume in the sample. Thus, the SEs is capable of producing high-resolution SEM micrographs of superior surface morphology contrast, whilst BSE micrographs reveal superior compositional contrast but with poorer spatial resolution (András E.Vladára, 2020).

2.9.5 UV–Vis diffuse reflectance spectroscopy

UV–Vis diffuse reflectance spectroscopy is one of the most employed methods for the determination of the optical band gap of materials. In general, the optical excitation of the electrons provokes an increase in absorbance at the wavelengths corresponding to the activation energy of the electrons, which allows determining the position of the absorption edge. To evaluate the optical bandgap from the absorption spectra, the Kubelka–Munk theory is commonly applied. This theory describes the behavior of the light path through a dispersing medium as a function of the scattering (S) and absorption (k) coefficients (Getaneh Diress Gesesse, 2020):

$$F(R\infty) = {(1 - R\infty)^2}\Big/{(2R\infty)} = \frac{k}{S} = \alpha$$

where F(R∞) is the Kubelka–Munk function corresponding to the absorbance, R∞ is the absolute diffuse reflectance at each wavelength of an infinitely thick sample referred to a non-absorbing standard, k is the absorption coefficient, S is the scattering coefficient, and α is the absorption coefficient of the material. The optical absorption spectra are characterized by the

presence of tail states nearby the valence and conduction bands, and the energy band gap is usually evaluated from the Tauc representation:

$$\alpha.\,h\nu = B(h\nu - E_g)^n \text{ or } F(R\infty)h\nu = B(h\nu - E_g)^n$$

where h is Planck's constant (4.136 1015 eV s^{-1}), B is an energy independent constant, hν is the photon energy (eV), E_g is the optical bandgap energy (eV), and n is a constant that determines the type of optical transition: n = 2 for indirect allowed transition; n = 3 for indirect forbidden transitions; n = ½ for direct allowed transition; and n = 3/2 for direct forbidden transitions .The E_g values can be obtained from the extrapolation of the linear least squares fit of $[F(R\infty)\,hv]^{1/n}$ to zero, by plotting $[F(R\infty)\,hv]^{1/n}$ vs hv (Jose Torrent, 2002).

CHAPTER THREE

3. Material and Methods

3.1 Apparatus and Instruments

The apparatus and equipment that used during this research work were Uv-Vis(T80+- PG instrument), Diffuse reflectance spectroscopy(Uv-Vis DRS Elico SL-150 spectrophotometer), XRD(Shimadzu,XRD-7000S South Korea), FTIR(FTIR Perkin Elmers spectrophotometer), SEM(Scanning Electron Microscopy), TGA(Thermogravimetric Analysis), electronic balance, oven, beaker, test tube, magnetic stirrer, thermometer, Whatman No.1, filter paper, measuring cylindr, pH-meter, spatula, Erlenmeyer flask, volumetric flask, ceramic crucible, buckner funnel, and bare magnet.

3.2 Chemical and Reagents

Chemicals used in experimental part of this work were presented in Table 2

Table 2: Chemicals used in experiments

	Name	Chemical Formula
1.	Sodium hydroxide	NaOH (Sigma aldria 99% purity)
2.	Hydro chloric acid	HCl (Riedel dehaen,Germeny,37 % HCl
3.	Ferrous Sulphate	$FeSO_4.7H_2O$ (Sigma aldria ,99% purity
4.	Ferric chloride	$FeCl_3.6H_2O$ (Sigma aldria ,99% purity
5.	di-Sodium hydrogen phosphate dehydrate	$Na_2HPO_4{\cdot}2H_2O$ (Sigma aldria ,99% purity
6.	Ammonium molybdate	$(NH4)_6Mo_7O_{24}{\cdot}4H_2O$ (Loba Chemie 99% purity)
7.	Ammonium metavanadate	NH_4VO_3 (Loba Chemie 99% purity)
8.	*Eucalyptus Globulus* leaf extract	

All chemicals mentioned in Table 2 and some additional materials were purchased from laboratory chemical suppliers, Addis Ababa, Ethiopia.

3.3 Preparation of *Eucalyptus Globules* extract

Fresh plant leaves of Eucalyptus Globules were collected and washed for removing dust and any impurities by using distilled water several times and dried at room temperature under shade. The dried flowers were chopped and then grinded into powder. Then, the grinded powders were sieved using 250 μm diameter sized sieve. The plant powder (5g) was extracted by boiling 100 ml of water in 250 mL glass flasks at 60 ^{0}C for 10 minutes. Then the resulted light yellow colored extract was cooled to room temperature and filtered before to remove any heavy biomaterials. Finally, the extract was kept at 4 ^{0}C in order to be used for the synthesis of the target magnetic nanoparticles.

3.4 Synthesis of Fe_3O_4 Nanoparticles Using Plant Extract

Fe_3O_4 NPs were synthesized based on co-precipitation method in the presence of aqueous leaf extract of *Eucalyptus globulus extract* as a capping agent. In a typical procedure, $FeCl_3 \cdot 6H_2O$ and $FeSO_4 \cdot 7H_2O$, were mixed in distilled water at 2:1 molar ratio then it followed by magnetic stirring. Then, the reaction was allowed for 15 min at 100 ^{0}C temperature with constant stirring under atmospheric condition. After that, the aqueous solution of *Eucalyptus globulus* leaf extract was added to the mixture with a rate 3 mL/min to make volume ratios of 1:1, 1:2, and 2:1 while stirring at room temperature for 10 min using magnetic stirrer. 8 M NaOH was added drop wise to the reaction mixture with rate of 3 mL/min until the pH become 11 to facilitate precipitation of Fe_3O_4 nanoparticles. Then black precipitate, of Fe_3O_4 NPs, was obtained and filtered by using Whatman No 1 filter paper. The product was washed with distilled water three times and dried for one hour in oven at temperature 80 ^{0}C for further use. The possible reaction is shown below.

$$2\ FeCl_3.6H_2O\ (aq) + FeSO_4 \cdot 7H_2O\ (aq) + 8\ NaOH\ (aq) + EGLE \rightarrow Fe_3O_4 \downarrow + 6\ NaCl\ (aq) + Na_2SO_4 + 17\ H_2O\ (aq) \quad \ldots\ldots\ldots\ldots\ldots\ldots\ldots\ldots\ (27)$$

3.5 Characterization of the Biosynthesized Fe_3O_4 Nanoparticles

The characterizations of the biosynthesized Fe_3O_4 nanoparticle were done by using TGA, FTIR, XRD, SEM, and UV-Vis DRS Spectrophotometer.

3.5.1 Characterization of Biosynthesized Fe_3O_4 NPs using TGA/DTA

Thermogravimetric analysis of the biosynthesized Fe_3O_4 nanoparticles was done at Bahirdar University Chemistry Department in flowing air atmosphere and the thermograms were recorded in the temperature range of 25–800 ^{0}C, at a heating rate of with a heating rate of 20 ^{0}C/min.

Sample preparation: A piece of specimen of powder (7 – 8 mg) was placed in a platinum basket and the temperature was continuously recorded by a thermocouple under the basket. While the sample was heated at a uniform rate in an appropriate environment, TGA measures the percent weight loss of a test sample.

3.5.2 Characterization of the Biosynthesized Fe_3O_4 NPs using XRD

X-ray diffraction (XRD) analysis of the synthesize nanomaterial was done at Adama Science and Technology University Material Science department. X-ray diffraction patterns of the dried powder of the biosynthesized Fe_3O_4 NPs samples were recorded on shimadzu XRD-7000 X-ray diffractometer, copper emission as X-ray source, with Ni filter, and wavelength of 1.5418 A. The samples were scanned in the 2θ range of 10–80 degrees, at a scanning rate of 3 deg/min.

Sample preparation: 1.5-2.5 gram of dried Fe_3O_4 NPs grinded by mortar and paste and then it was filled into the sample holder and subjected into X-ray diffractometer.

3.5.3 Characterization of the Biosynthesized Fe_3O_4 NPs using FTIR

FTIR analysis of the synthesize nanomaterial was done at Addis Ababa University Chemistry Department. FTIR spectrum of the dried powder of the biosynthesized Fe_3O_4 samples were recorded on 65 FT-IR (PerkinElmer) in the range 4000-400 cm^{-1}.

Sample preparation: The synthesized powders of the nanomaterial were mixed with potassium bromide (KBr) as dilute to form a very fine powder. The powder was then compressed into a thin transparent pellet which was used for recording FTIR spectrum.

3.5.4 Characterization of Fe_3O_4 NPs using SEM

SEM analysis of the biosynthesized Fe_3O_4 NPs were carried out at Addis Ababa Science and Technology University Chemistry Department which reveals information about the external morphology of the biosynthesized Fe_3O_4 sample with direct visualization.

Sample preparation: Small amount of powder sample was dispersed in acetone and sonicated for few minutes. Some samples were needed to be coated to make them conductive. Metals require no preparation due to their inherent ability to conduct electricity. However, non-metals need to be coated with a conductive material such as gold/ gold-palladium alloy, using a sputter coater.

3.5.5 Characterization of the Biosynthesized Fe_3O_4 NPs using UV-Vis DRS Spectrophotometer

The optical properties and band gap energy of EGLE coated magnetite nanoparticles were characterized by UV-Vis DRS spectrophotometers at Adama Science and Technology University Material Science Department. The range of absorption was between 250 nm to 950 nm.

Sample preparation: Finely ground powder of a standard ($BaSO_4$) and sample were carefully packed into a sample holder with a rectangular or circular hole with a surface of a few tens square millimeters to several square centimeters. Then the holder was placed horizontally at the bottom of the integrating sphere and diffuse reflectance spectra was recorded.

3.6 Adsorption Study of Phosphate by Biosynthesized Fe_3O_4 Nanoparticles

3.6.1 Stock solution preparation

In this experiment stock solution with the di-Sodium hydrogen phosphate dehydrate ($Na_2HPO_4 \cdot 2H_2O$) concentration of 220 mg/l was prepared. Concentrations of phosphorus in all experiments were checked using Vanadomolybdophosphoric acid Colorimetric method by using Azzota Double beam UV-VIS spectrophotometer in Biology Department in Adama Science and Technology University.

Principle: In a dilute orthophosphate solution, ammonium molybdate ($(NH_4)_6Mo_7O_{24} \cdot 4H_2O$) reacts under acid conditions to form a heteropolyacid, molybdophosphoric acid. In the presence of vanadium, yellow vanadomolybdophosphoric acid is formed. The intensity of the yellow color is proportional to phosphate concentration. Positive interference is caused by silica and arsenate only if the sample is heated. Negative interferences are caused by arsenate, fluoride, thorium, bismuth, sulfide, thiosulfate, thiocyanate, or excess molybdate. Blue color is caused by ferrous iron but this does not affect results if ferrous iron concentration is less than 100 mg/L. The wavelength at which color intensity is measured depends on sensitivity desired, because sensitivity varies tenfold with wavelengths 400 to 490 nm. Ferric iron causes interference at low wavelengths, particularly at 400 nm. A wavelength of 470 nm usually is used (William Nivens, 2018).

3.6.2. Bach Adsorption Experiment

All batch experiments were carried out at a constant temperature 25 $\pm 2^0$C. The designed solution pH was adjusted using 0.1 M NaOH and HCl. A known amount of adsorbent was added to samples and mixed and allowing sufficient time for adsorption equilibrium. The parameters like initial phosphate ion concentration, pH, contact time and sorbent dosage were chosen as independent variables and the removal efficiency of phosphate was considered as output response.

The analysis focused on how the removal efficiency was influenced by independent variables, phosphate concentration (X_1), pH (X_2), contact time (X_3), and sorbent dosage (X_4). The dependent output variable was maximum removal efficiency (Y). The experiment was optimized based on the study of (Heng Xiang C. L., 2014). The adsorption experiment was conducted by varying pH (1-6) and at pH of 8,10,12,14 for basic pH range. The optimization also was done by varying adsorbent dosage (0.25 g/L, 0.5.g/L, 1 g/L, and 2 g/L) and contact time (20 min, 40 min, 60 min, 80, min, 100 min and 120 min) to get maximum adsorption of the phosphate by Fe_3O_4 NPs.

To test the effect of one parameter other parameters were kept constant. After adsorption, the magnetic biosorbent were separated from the solutions using a Whatman No 1 filter paper, and the initial and final metal concentrations were determined. The equilibrium adsorption capacity (q_e) was calculated according to the following equation

$$q_e = \frac{(C_O - C_e)V}{w} \quad \ldots\ldots\ldots\ldots\ldots\ldots\ldots (28)$$

Where, q_e is the equilibrium adsorption capacity per gram dry weight of the adsorbent, mg/g; C_0 is the initial concentration of phosphate in the solution (mg L^{-1}); C_e is the final or equilibrium concentration of phosphate in the solution (mg L^{-1}); V is the volume of the solution (L), respectively. The removal percentage was determined by

$$E = \frac{(C_O - C_e)}{C_O} * 100 \quad \ldots\ldots\ldots\ldots\ldots\ldots\ldots (29)$$

Where, C_o and C_e represent the initial concentration and final concentration (mg/l), respectively.

3.6.3 Adsorption kinetics Study

Adsorption kinetics is used to understand absorption mechanisms and effect of contact time on the adsorption. In to each sample of 5 mg/L, 10 mg/L, 15 mg/L, 15 mg/L, 25 mg/L solution of phosphorus, 1 g of magnetite was added followed by using stirring rod at 100 rpm at pH =6.10 ml samples were taken after the following time intervals: 20 min, 40 min, 60 min, 80 min, 100 min, and 120 min. Samples were filtered to remove magnetite particles and then diluted and measured using cuvette tests.

3.6.4 Adsorption isotherm of phosphorus on magnetite

Equilibrium isotherms were obtained as follows. A number of solutions with different known Phosphate concentrations (5 mg/L, 10 mg/L, 15 mg/L, 20 mg/L, and 25 mg/L) and same volume (50 ml) were prepared and transferred to separate beakers. During continuous mixing on the stirring rod, 1g/L of magnetite was added to each sample. After stirring for 10 min the beakers were placed for 120 min in order to settle magnetite particles. Samples were taken from the upper clear part of the solution then diluted and equilibrium concentrations were measured using cuvette tests.

3.6.5 Desorption Study

The reversibility of phosphate ions adsorption on Fe_3O_4 NPs was investigated using NaOH (1 M) as desorption agent. Desorption experiments were conducted using the following procedures. At first, six samples of 50 ml of phosphate solution with initial phosphate concentration of 25 mg/L, pH 6, and 50 mg of the adsorbent were added and after 120 min, solution was filtered. For desorption purpose,45 ml of distilled water were added to sorbent then NaOH solution (1 M) were added to the solution to adjust the pH of the solution in between 8-14 and mixed by stirring rod for 30 minute. After 6 hour the solution were filtered and the residual concentration of phosphate ions in the solution were determined to evaluate phosphate recovery by the following equation.

$$\text{Desorption efficiency } (\%) = \frac{C_{des}}{C_{ads}} \times 100$$

Where C_{ad} denotes the concentration of phosphate ions adsorbed and C_{de} is the concentration of phosphate ions desorbed (Jonas Bayuo, 2020).

CHAPTER FOUR

4. Results and Discussion

4.1 Observed results during the biosynthesis of Fe_3O_4 NPs

When $FeCl_3.6H_2O$ and $FeSO_4.7H_2O$ were dissolved in water a light brown color was observed. After heating of the mixture at 100 ^{0}C for 15 minute followed by the addition of EGLE at volume a ratio of 1:1, 1:2, and 2:1 the color of the solution is changed into black. This is most probably due to the reaction between the polyphenol found in the EGLE and the iron solution (Ting Wang, 2014). Then the precipitation of Fe_3O_4 NPs starts to occur after the addition of 8M NaOH. When NaOH is added to the solution it starts to precipitate at pH around 8.5 and the precipitation process continues up to pH of 11. Precipitation of nanomaterial is occurring due to mixing of a solution containing a particular cation (a positively charged ion) with another solution containing a particular anion (a negatively charged ion) involve the exchange of parts between the two reactants. The possible reaction mechanism in the synthesis of EGLE coated Fe_3O_4 NPs is described by (Nene Ajinkya, 2020).

$$2FeCl_3 + FeSO_4 + 8\ NaOH \xrightarrow{EGLE} Fe_3O_4 \downarrow + 6\ NaCl + Na_2SO_4 + 4\ H_2O \ldots\ldots\ldots\ldots\ldots (30)$$

4.2 Thermogravimetric analysis of biosynthesized Fe_3O_4 NPs

The thermogravimetric curves for the thermal decomposition (TGA/DTA) of the biosynthesized Fe_3O_4 mixture Figure 5 reveal three steps of mass loss. These thermal events are associated with the degradation of the main components of the mixture. The first weight loss of about -7.54 % happened at 100 °C, and an endothermic peak was detected at approximately 76.19°C, which was related to the evaporation of H_2O on the surface and precursor building .while the second weight losses reported to be 5.8 %occurred in the temperature range 110 -382 ^{0}C is associated with the degradation of capping materials and organic compounds (Marluce Oliveira da Guarda Souza, 2020). Such processes are exothermic, as evidenced by the peaks in the DTA curve, at the temperatures 289.82 ^{0}C and 363.17 ^{0}C. In the last step There were no signs of any specific weight losses throughout the

range of 441– 800°C and two exothermic peaks are observed in the DTA curve at 615.5 ^{0}C and 691 ^{0}C (Zahra Sabouri, 2021).

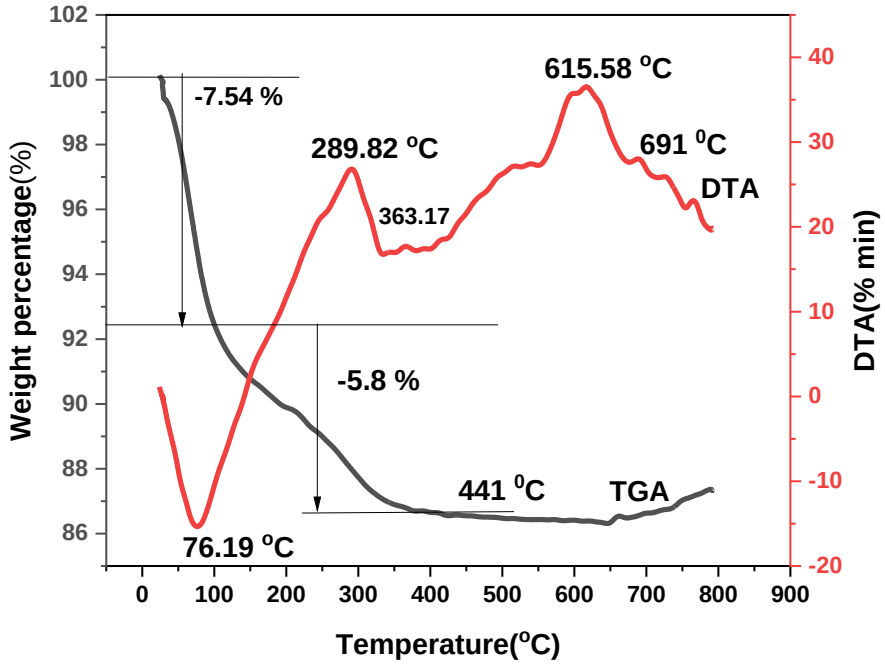

Figure 5: TGA curve of Biosynthesized synthesized Fe_3O_4 NPs

According to the (NuchareeNucharee Chomchoey, 2018) the synthesized MNPs dried in oven at 80°C (Figure 6a) are black in color and strongly attracted by a laboratory bar magnet. This MNP with ferromagnetic behavior is most probably magnetite (Fe_3O_4), while the dark brown color obtained with calcination at 441^{0}C (Figure 6b) may indicates the presence of maghemite (γ-Fe_2O_3), which is formed by the oxidation of magnetite. The brick red color is obtained after calcination at 600^{0}C (Figure 6c) is most probably from hematite (α-Fe_2O_3) formed by inversion of maghemite at temperatures 600 ^{0}C. However, it must be kept in mind that the apparent color of MNP particles represents only particles at surface. Such particles may have a core-shell structure, for example with a surface layer (shall) of dark brown maghemite and the inner core of magnetite. For such cases the magnetic examinations can provide more informative than the superficial optical observations.

Figure 6: Photograph of the Biosynthesized synthesized Fe_3O_4 after calcination in air at a) 80 ^{0}C, b) 441^{0}C, c) 600 ^{0}C

4.3 X-ray diffraction analysis of biosynthesized Fe_3O_4 NPs

Figure 7 shows XRD diffractograms for calcined and uncalcined biosynthesized magnetite nanoparticle in 1:1, 1:2 and 2:1 ratios, respectively, with sharp characteristic peaks at 2θ values of 30.28, 35.52, 43.1, 53.6, 56.94, and 62.58 showing the crystalline nature Fe_3O_4 nanoparticles. Figure 7 (b, c and d) shows the XRD spectrum of calcined Fe_3O_4 NPs and Figure 7 (a) shows uncalcined Fe_3O_4 NPs both synthesized from ferric chloride hexahydrate and ferrous sulphate heptahydrate as precursor and eucalyptus leaf extract in 1:1, 1:2 and 2:1 ratios.

The X-ray diffraction patterns all of the samples at 2θ (degree) correspond with hkl plane in a crystal lattice i.e., (2 2 0), (3 1 1), (4 0 0), (422), (5 1 1), and (4 4 0). Three maximum of peaks at 2θ of 30.24°, 35.52°, and 62.8 ° with a narrow peak and All the observed diffraction peaks shows the formation of Fe_3O_4 structure and are matched with the literature value (JCPDS Card No: 42-1468) mentioned (Azza M. Mazrouaa, 2019).

For the four NPs, all the observed peaks can be taken as confirmation for formation of Fe_3O_4 NPs. An additional peak observed at 2θ values of 18.31^0, 33.17^0, 49.52^0 might be due to the presence of trace amount of γ-Fe_2O_3 and β-Fe_2O_3 NPs (Raja Das, 2019).

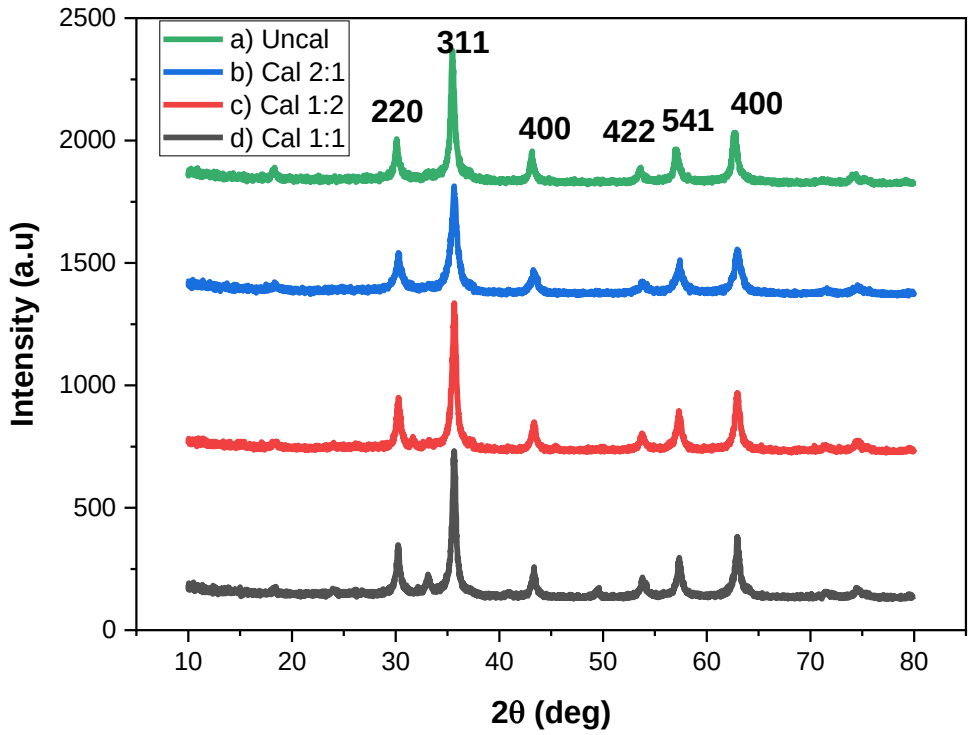

Figure 7: XRD Pattern of Biosynthesized Fe3O4 NPs of (a) uncalcined Fe_3O_4 NPs. (b) Cal 2:1 Fe_3O_4 NPs, (c) Cal 1:2 Fe_3O_4 NPs, and (d) Cal 1:1 Fe_3O_4 NPs

Crystallite size generally corresponds to the coherent volume in the material for the respective diffraction peak. Sometimes, it also corresponds to the size of the grains of a powder sample, or thickness of polycrystalline thin film or bulk material. The Scherrer's equation is used for determination of size of particles of crystals in the form of powder, which can be represented as follows:

$$d = {}^{k\lambda}/_{\beta cos\theta} 1.5416 \ldots\ldots\ldots\ldots\ldots\ldots\ldots\ldots \quad (31)$$

As it can be observed from Table 3, the average crystal sizes of the biosynthesized Fe3O4 are all lie in the nano-range size. According to (Narayanaswamy, et al., 2021) the difference in the sizes of the particles that is shown in Table 3 can be attributed to the iron salt concentration dependent competing nucleation and growth processes and the electrostatic repulsion effect during the particle formation reaction.

A high concentration of ions in the initial solution can produce smaller particle sizes due to higher electrostatic repulsion for the species migrating towards a growing particle. Whereas at lower concentrations of ions, the electrostatic repulsion factor is relatively less dominant, and the particle growth in such cases is primarily limited by the diffusion of species from solution to the growing surface of a particle.

The magnitude of the distance between two adjacent and parallel planes of atoms (i.e., the interplanar spacing d_{hkl}) is a function of the Miller indices (*h*, *k*, and *l*) as well as the lattice parameter (α). For example, for crystal structures those have cubic symmetry (Mate William D. CallisterJR, 2018)

$$d_{hkl} = {\alpha}/{\sqrt{h^2 + k^2 + l^2}} \quad \text{..... (32)}$$

The calculated lattice parameters of synthesized EGLE coated Fe_3O_4 NPs were in between α=8·35Å - 8.384Å, respectively. This result were in good agreement with the standard data (JCPDS: 19-0629) lattice parameter of Magnetite NPs (α =8·39 Å).

Table 3: Interplanar spaces (d-hkl), FWHM values, lattice parameter, and crystallite sizes of Biosynthesized Fe_3O_4 NPs.

Calcinated Fe_3O_4 NP Size 1:1									
2θ value(deg)	Θ Value (deg)	θ value in rad	d_{hkl}(Å)	hkl value	$(h^2+k^2+l^2)^{1/2}$	FWHM Value in(deg)	FWHM Value in (rad)	lattice parameter (α) in Å	crystallite sizes in nm
30.28039	15.1402	0.26424625	2.9516	220	2.83	0.60592	0.0106	8.35298	13.5932
35.64921	17.8246	0.31109805	2.5184	311	3.32	0.62957	0.011	8.36117	13.2652
43.34085	21.6704	0.37822027	2.0876	400	4	0.52135	0.0091	8.35059	16.4096
53.80939	26.9047	0.46957551	1.7036	422	4.9	0.57427	0.01	8.34772	15.5249
57.332	28.666	0.50031608	1.607	511	5.2	0.66311	0.0116	8.35659	13.6645
62.96526	31.4826	0.54947555	1.4761	440	5.66	0.6851	0.012	8.35496	13.608
Average Value								8.354	14.3442
Calcinated Fe3O4 NP Size 1:2									
2θ value	Θ Value (deg)	θ value in rad	d_{hkl}(Å)	hkl value	$(h^2+k^2+l^2)^{1/2}$	FWHM Value in(deg)	FWHM Value in (rad)	lattice parameter (α) in Å	crystallite sizes in nm
30.12261	15.0613	0.26286936	2.9667	220	2.83	0.65918	0.0115	8.39572	12.4902
35.49896	17.7495	0.30978687	2.5287	311	3.32	0.61651	0.0108	8.39541	13.5405
43.151	21.5755	0.37656351	2.0964	400	4	0.51181	0.0089	8.38557	16.7045
53.59521	26.7976	0.46770644	1.7099	422	4.9	0.50336	0.0088	8.3786	17.6952
57.10169	28.5508	0.49830625	1.613	511	5.2	0.60956	0.0106	8.38744	14.8487
62.71134	31.3557	0.54725968	1.4815	440	5.66	0.68996	0.012	8.38532	13.4938
Average Value								8.38801	14.7955
Calcinated Fe_3O_4 NP Size 2:1									
2θ value	Θ Value (deg)	θ value in rad	d_{hkl}(Å)	hkl value	$(h^2+k^2+l^2)^{1/2}$	FWHM Value in(deg)	FWHM Value in (rad)	lattice parameter (α) in Å	crystallite sizes in nm
30.28032	15.1402	0.26424564	2.9516	220	2.83	0.97127	0.017	8.353	8.47999
35.63971	17.8199	0.31101514	2.5191	311	3.32	0.92555	0.0162	8.36332	9.02289
43.34876	21.6744	0.37828929	2.0873	400	4	0.70333	0.0123	8.34914	12.1641
53.84619	26.9231	0.46989665	1.7025	422	4.9	0.63355	0.0111	8.34244	14.0746
57.37634	28.6882	0.50070302	1.6059	511	5.2	0.88532	0.0155	8.35068	10.237
62.99755	31.4988	0.54975733	1.4755	440	5.66	0.90901	0.0159	8.35112	10.2578
Average Value								8.35162	10.706
UnCalcinated Fe_3O_4 NP Size 1:1									
2θ value(deg)	Θ Value (deg)	θ value in rad	d_{hkl}(Å)	hkl value	$(h^2+k^2+l^2)^{1/2}$	FWHM Value in(deg)	FWHM Value in (rad)	lattice parameter (α) in Å	crystallite sizes in nm
30.24871	15.1244	0.26396979	2.9546	220	2.83	0.57093	0.01	8.36153	14.4251
35.63476	17.8174	0.31097195	2.5194	311	3.32	0.55559	0.0097	8.36445	15.0309
43.32996	21.665	0.37812523	2.0881	400	4	0.5383	0.0094	8.35259	15.8923
53.88039	26.9402	0.4701951	1.7015	422	4.9	0.62787	0.011	8.33754	14.204
57.36222	28.6811	0.5005798	1.6063	511	5.2	0.58512	0.0102	8.35256	15.4881
62.97409	31.487	0.54955261	1.476	440	5.66	0.65202	0.0114	8.35391	14.299
Average Value								8.35376	14.8899

4. 4 FTIR analysis of biosynthesized Fe_3O_4 NPs

The FTIR spectra of synthesized Uncalcined Eucalyptus coated Magnetite and Calcined Eucalyptus coated Magnetite NPs samples were shown in Figure 8.In Figure 8 (a) The FTIR spectrum of green synthesized uncalcinated iron oxide magnetite nanoparticles showed peaks at 3686, 2992, 1684, 1520, 1400, 1214, 1223, 926 and 565 cm^{-1}. The FTIR spectrum at 3686 cm^{-1} corresponds to the presence of O-H stretching indicating the existence of small amount of water adsorbed to the NPs (Sirajunnisa Abdul Razack, 2019). The peak around 2992 cm^{-1} is assigned to residual organic component in the C≡H stretch mode frequencies, respectively (Shraddha Chauhan, 2019). The peak around 1844 cm^{-1} can also be carbonyl (C = O) stretching vibration (Henam Sylvia Devi, 2017) and the absorption band around 1550 cm^{-1} corresponds to asymmetric stretching of C=C bonds (Alagumira Meyyappan, 2014). The peak around 1400 $cm^{-1}$and 1223 cm^{-1}could is due to bending vibration of C-N stretch and C-O stretching of bonds. The peak appearing at around 594 cm^{-1} was assigned to the metal-oxygen (Fe–O) stretching modes (M. Nurbasa, 2017).

Figure 8 (b) shows the FT-IR spectrum of calcinated synthesized Fe_3O_4 NPs showed peaks at 3690, 2992, 1840, 1686,1550, 1407,1290,926,743, and 643cm^{-1}. The broad stretching absorption peaks of magnetite nanoparticles observed at 3690 cm^{-1} can be due to the intermolecular H-bonded OH functional group. The peak at 2992 cm^{-1} represents characteristic of the stretching vibration of C≡H functional group (Derya Aksu Demirezen, 2019). The peak at 1840 cm^{-1} was attributed to the stretching vibrations of C = O functional group. The absorption band around 1686-1550 cm^{-1} corresponds to asymmetric stretching of C=C bonds. The absorption peak at 1412-1300 cm^{-1} can be assigned to stretching vibration for aromatic amines (Ting Wang, 2014). The absorption peak at 1227 cm^{-1} can be assigned to the presence of C-O stretching. Absorption peak appeared at 926 cm^{-1} and 743 cm^{-1} conferring the presence of moisture of C=C bending group in the sample. Furthermore, adsorption bands at around and 643 cm^{-1} refer to Fe-O stretches of Fe_3O_4 (M. T. Hossain1, 2018).

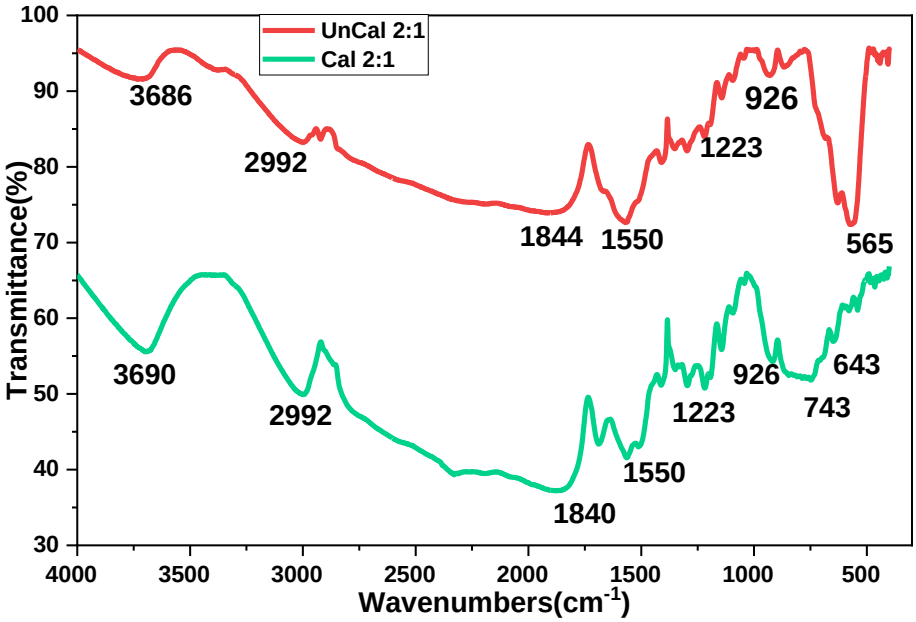

Figure 8: FTIR spectra of Biosynthesized (a) Calcined Fe_3O_4 NPs (b) UnCalcined Fe_3O_4 NPs

4. 5 UV-Vis DRS analysis of biosynthesized Fe_3O_4 NPs

The optical absorption property of calcinated EGLE coated Fe_3O_4 NPs powders were analyzed by the diffuse reflectance measurements. The diffuse reflectance spectrum of sample Fe_3O_4 NPs indicates that a sharp increase of the reflectance in the range of 400-800 nm, typical for Fe_3O_4 nanopowders with a reddish brown color. According to (Toda, 2018)for smaller particle a size, the absorbed component by the powder layer is smaller, as the relative reflecting surface increases. That is to say that light cannot penetrate deeply into the powder layer. Moreover, particles with a diameter smaller than the wavelength of light would engender wavelength dependence in scattered light. The Figure 9 confirms the visual observations concerning the color change to the reddish brown as a consequence of carbon removal during calcination process as reported by (Robert Ianos, 2018).

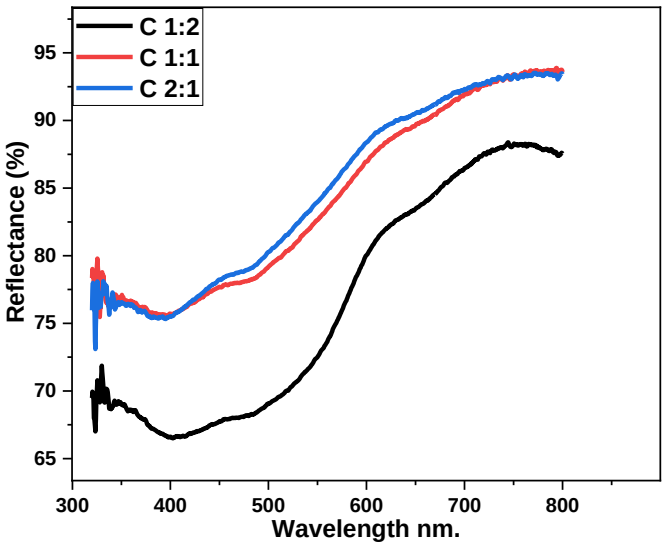

Figure 9: (a). % of Reflectance of Biosynthesized Magnetite NPs at different ratio

Figure 10 depicts the results of Kubelka-Munk (K-M) model and the F(*R*) is estimated using the formula, $F(R) = (1-R)^2/2R$, where F(*R*) is the Kubelka-Munk function, and *R*, is the reflectance. The extrapolation in the linear region of the plot gives an energy band gap (Qi Li1, 2014). the Tauc Plot $(F(R)\ hv)^n$ vs. hv) to determine the Fe_3O_4 NPs band gap so that The band gap energy of nanomaterial is 1.89 eV, 1.92 eV and 2.19 eV for average magnetic nanoparticles of 14.79 nm, 14.34 nm and 10.70 nm, respectively. The band gap values of EGLE coated Fe_3O_4 NPs were greater than its bulk value.

These results show that the energy band gap of Fe_3O_4 NPs may depend on its particle size. This can be explained quantum mechanically as the particle size reaches the nanoscale, the number of overlapping of orbitals or energy level decreases and the thickness of band becomes thinner. This will cause a rise in energy band gap between the valence band and the conduction band (Madan Singha, 2018).

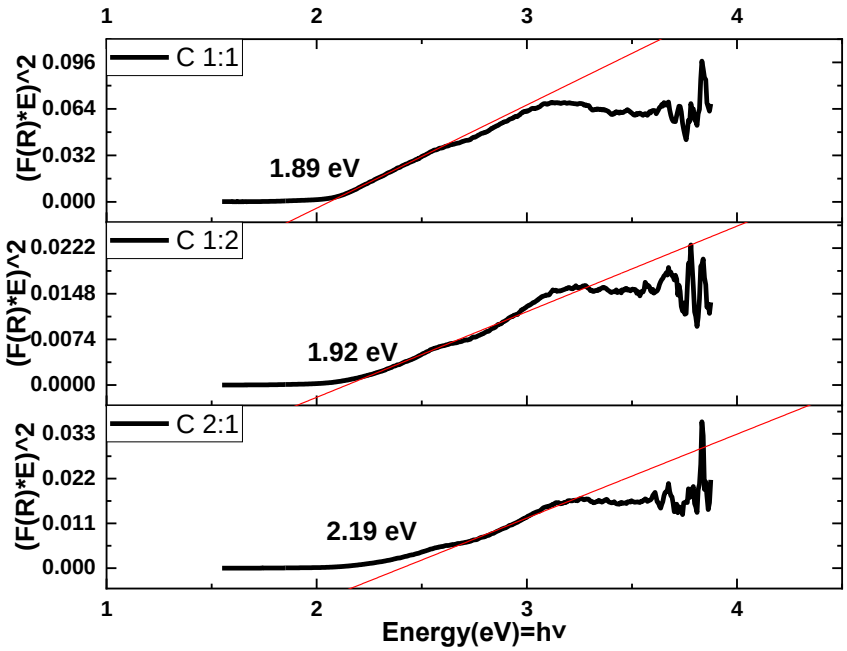

Figure 10: (b) Tauc plot for Biosynthesized Magnetite NPs at different ratio

4. 6 SEM analysis of biosynthesized Fe_3O_4 NPs

Scanning electron microscope is one of the most widely used techniques used in characterization of nanomaterials and nanostructures. The signals that derive from electron-sample interactions reveal information about surface morphology (texture), of the sample. Figure 11 shows aggregations of Fe_3O_4 nanoparticles which are observed by low magnification SEM analysis instrument. As observed from SEM image (Figure 11), calcinated Fe_3O_4 with 2:1 ratio is more aggregated than calcinated 1:1 and 1:2 NPs. According to (W.Zhang, 2014) smaller particles are more susceptible to aggregation at the same conditions as evidenced by many study. As particle decreases in size, a greater percentage of its atoms exist on the surface.For instance, a decrease in size will lead to a larger relative surface energy that would destabilize the system. The smaller the particle, the higher the surface energy, thus smaller particles aggregate more readily than larger particles because aggregation will lower the free energy of the system.

Also From SEM image analysis of the nanomaterial we can observe that the particle distribution of the nanomaterial in the ranges between 2.94-8.61 µm for 2:1 Fe_3O_4, 2.14-5.60 µm for 1:1 Fe_3O_4, and 1.18 – 5.00 µm for 1:2 Fe_3O_4 NPs.

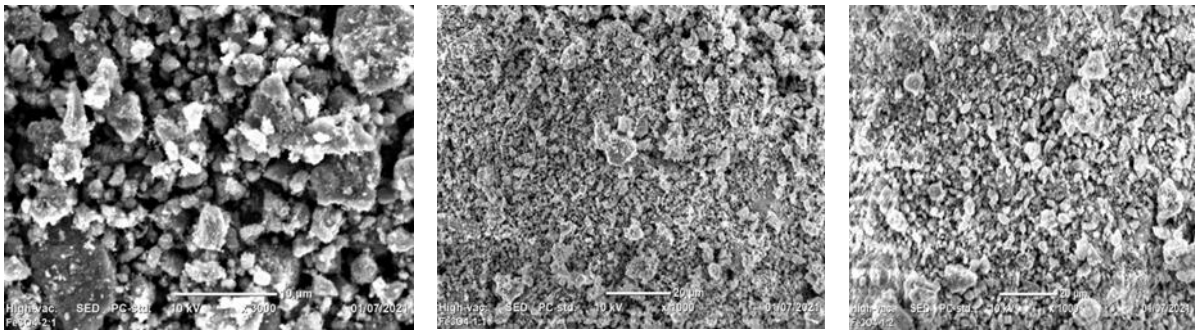

Figure 11: Scanning Electron Microscopy Image of Biosynthesized a) Fe_3O_4 (2:1), b) Fe_3O_4 (1:1) and c) Fe_3O_4 (1:2) ratio

4.7 Adsorption Study Experiment

Calibration curve for standard solution were done by various concentrations (0.2 mg/L, 0.6 mg/L, 1 mg/L, 1.5 mg/L, 2 mg/L) as shown in Table 4. The experiments were repeated four times and the average data were used to plot the resultant graphs. A calibration curve of absorbance against phosphate concentrations was then plotted (Figure 13). The experimental data reported in Figure 12 were fitted by a straight line with a high regression coefficient value (R^2= 0.9218)

Table 4: the calibration curve data for phosphate

Conc(X)	Absb(1)	Absb(2)	Absb(3)	Absb(4)	Absrb 5	Avg
0.2	0.023	0.023	0.017	0.023	0.062	0.0296
0.6	0.025	0.027	0.019	0.026	0.069	0.0332
1	0.027	0.031	0.02	0.024	0.075	0.0354
1.5	0.028	0.033	0.035	0.027	0.125	0.0496
2	0.03	0.036	0.024	0.04	0.192	0.0644

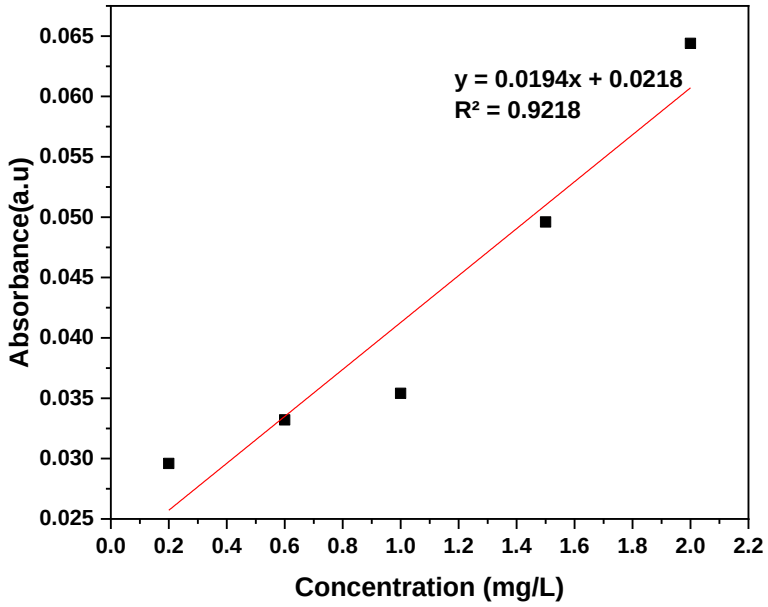

Figure 12: Calibration Curve for standards Samples

4.7.1 Effect of pH on Adsorption of Phosphate

The pH is one of the important factors in phosphate removal using Fe_3O_4nanoparticle from wastewater. It has been reported that the solution pH can alter the adsorption/desorption of phosphate to/from iron oxide-based materials by changing the amount of charge and the charge characteristics of the phosphate and the surface of the materials and further changing the dominant adsorption/desorption mechanisms. In this part, the effect pH on metal adsorption was studied putting 1 g of biosynthesized Fe_3O_4 nanoparticle at 1:1, 1:2 and 2:1 ratios on 25 mg/l of phosphate solution for contact time of 120 minute. The pH was regulated using 0.1 M HCl or 0.1 M NaOH solutions. The amount of phosphate removal decreases noticeably with the increase of pH values as showed in Figure 13. When the solution pH rises, the amount of positive charge on the surface of the magnetite particles with both sizes decreases, and the surface will finally become negatively charged when the solution pH is above the value of pH_{PZC} (7.9 for Fe_3O_4) (Hayton, 2018).

When the solution pH is above 7.9, the electrostatic attraction will change into electrostatic repulsion, which will significantly decrease/increase the adsorption/desorption of the phosphate to/from Fe_3O_4 NPs. The higher the pH, the lower/higher the adsorption/desorption of phosphate to/from the nanometer-sized magnetite particles (Mamun Rashid N. T., 2017).

When the solution pH is around 3, the electrostatic attraction between the positively charged magnetite surface and the negatively charged phosphate will drive the formation of an outer-sphere complex, which provides the strong adsorption and weak desorption behavior of the phosphate. At lower pH, sorbent surface will be positively charged while the phosphate species will be predominantly monoanionic i.e. $H_2PO_4^-$ (Mamun Rashid N. T., 2017).

Thus electrostatic attraction between H_2PO_4 and Fe_3O_4 NPs nanomaterial results in higher adsorption of phosphate onto magnetite nanoparticles but when the pH < 2 the adsorption of phosphate is relatively very low, this could be due to the presence of more hydrogen ion in the solution which results some part of magnetite to dissolve and the release of some part of phosphate to the solution. Moreover phosphate still has a certain degree of adsorption on magnetite when the solution pH is above the pH_{PZC} and the outer-sphere complex effect cannot be formed. This is because under a certain pH, the protonated iron surface groups with phosphate can form an inner-sphere complex such as the bidentate binuclear phosphate complex, which may result in a reduced desorption of phosphate from the magnetite particles (Lei Hou Q. L., 2020).

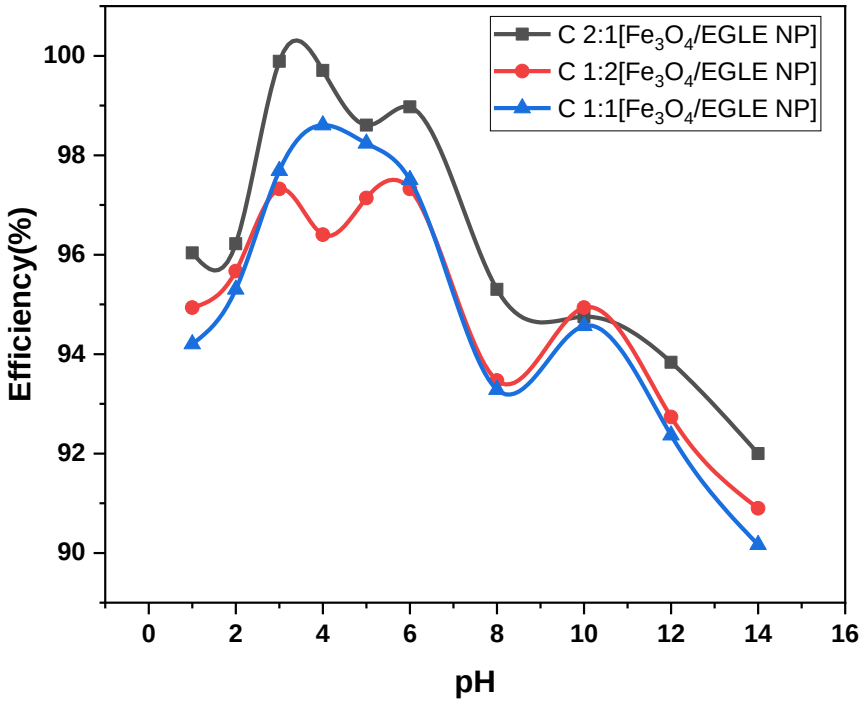

Figure 13: Effect of pH on removal efficiency of phosphate ion

4.7.2 Effect of Adsorbent Dosage on Phosphate Removal

Adsorbent dosage is one of the most important actions, to determine the adsorption capacity of adsorbent under specific operating conditions. This is also valuable from an economical point of view as it provides the idea of maximum adsorption of dye using a minimum dosage of the adsorbent (Suprakas SinhaRay, 2020).The effect of adsorbent dose was investigated by adding different dosage of adsorbent (0.25 g/l, 0.5.g/l, 1 g/l, 1.5 g/l, and 2g/l) on 25 mg/L phosphate for contact time of 120 min and pH =6 for all batch experiments. The removal of phosphate at different doses is shown in Figure 14.The results show that the removal percent increased with increasing adsorbent dose due to the increase in the total available surface area of the adsorbent particles (Malihe Pooresmaeil, 2020). At equilibrium the percentage of phosphate removal was increased from 94.18 % to 96.76 % with the increase of adsorbent mass from 0.025 g/L to 2 g/L, respectively. This is due to the extent of adsorption is directly proportional to the adsorption sites which is nothing but the amount of dosage.

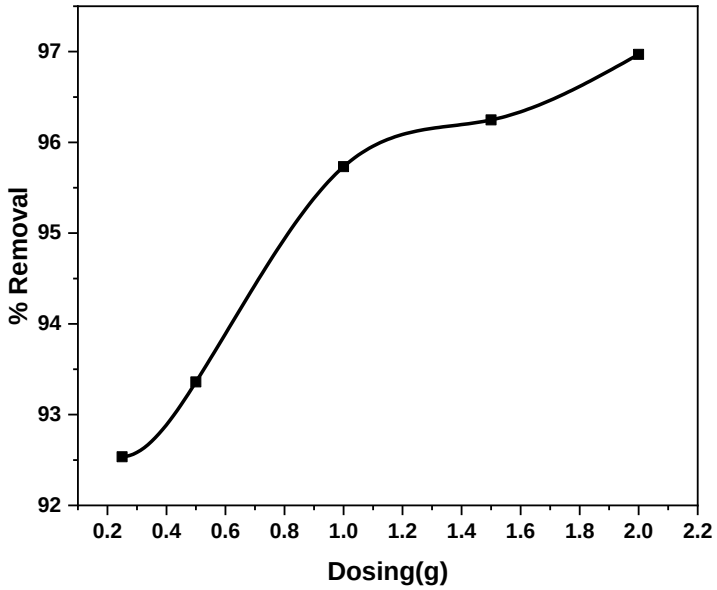

Figure 14: Percentage removal of phosphate as a function of adsorbent dosage (g/L) of Fe_3O_4 NPs.

4.7.3 Effect of initial concentrations of phosphate

The influence of different initial phosphate concentrations (5, 10, 15, 20,and 25 $mg \cdot L^{-1}$) on the removal efficiency of phosphate was studied using the same mass of biosynthesized Fe_3O_4 at a pH of 6 for 120 min. adjusting the phosphate solution pH to 6.1 g/L of adsorbent sample was added to solution and adsorbed for 120 min. According to (Hasfalina Che Man, 2012), the effect of initial concentration of adsorbate on the percentage of phosphate removal can be explained in terms of the number of exchangeable sites in adsorbent structure and phosphate-to-adsorbent ratios. Therefore, the reason for a decrease in percentage of removal with increasing initial concentration of adsorbate in this study is that as the ratio of phosphate to Fe_3O_4 NPs increases, the exchangeable sites in Fe_3O_4 NPs structure are saturated, resulting in a decrease of the removal percentage. As it is shown in Figure 15, the amount of phosphate adsorbed decreased with the increase in initial concentration. The ratio of available surface to initial phosphate concentration, at lower concentration was larger. Therefore, the adsorption became dependent on initial concentration.The percentage of phosphate removal was 97.5 % at 5 mg/L phosphate solution, which decreases slightly to 83.56 % at 25 mg/L of phosphate solution.

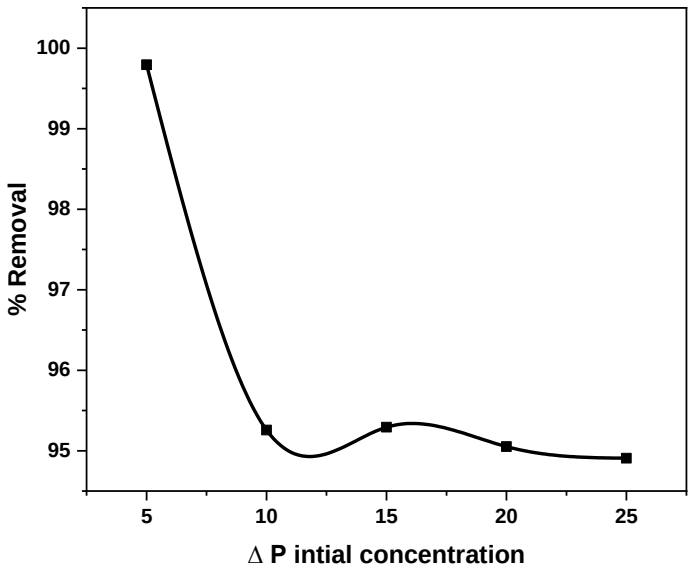

Figure 15: Influence of initial concentration of phosphate ions on removal efficiency

4.7.4 Effect of Contact time

Studies of contact time are helpful in understanding the amount of phosphate adsorbed by a fixed amount of the adsorbent at room temperature. Adsorptions can be assumed to be complete when equilibrium is achieved between the solute of solution and the adsorbent. However, specific time is needed to maintain the equilibrium interactions to ensure that the adsorption process is complete (Saidur Rahman Chowdhury, 2010). The adsorption experiments were carried out for different contact times with fixed sorbent dose, pH, and initial concentration. The effect of contact time on the adsorption efficiency of the Fe_3O_4 NPs with 25 mg/L of phosphate, pH=6 and contact time (20 min,40 min,60 min,80 min,100 min, and 120 min) is presented in Figure 16.Results showed that the removal seemed to take place in two phases. The first phase involved rapid metal uptake within 60 min of contact time and was followed by the subsequent slower uptake. The rapid adsorption of phosphate by magnetite mixture may be attributed to the external surface adsorption, and it is easy for phosphate to access active adsorption sites, thus resulting in a rapid uptake of phosphate. However, with increase in contact time the system attains a steady state. Afterwards the gradual occupancy of remaining vacant sites become difficult due to the repulsive force between the phosphate ions adsorbed on the surface and the adsorbate in the solution (H.Pandaa, 2017).

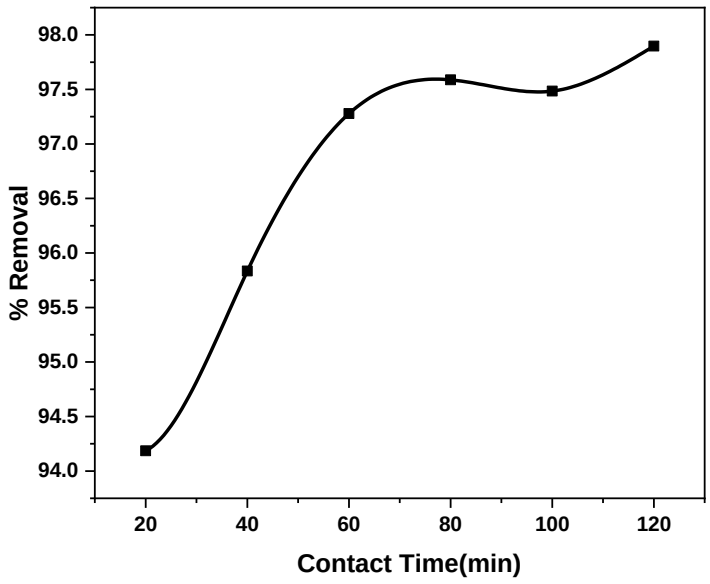

Figure 16: Percentage removal of phosphate as a function of contact time (min) by Fe_3O_4 NPs.

4.8 Adsorption kinetics Study

Adsorption kinetics is the study of the adsorption process rate. The controlling step and mechanism of the adsorption process are determined by study of the adsorption kinetics. Adsorption commonly occurs in three steps: (1) migration of adsorbate molecules to the outer surface of adsorbent, (2) diffusion of adsorbate to the boundary layer, and (3) finally diffusion from the adsorbent surface into internal adsorbent sites via pore diffusion.The pseudo first order (PFO) kinetics and pseudo second order (PSO) kinetics, kinetics models are commonly used models for study of the rate and mechanism of the adsorption process. The fitness of the adsorption mechanism with each of the models is determined by the coefficient of determination (R^2) (Ruixi Bai, 2017).

4.8.1 Pseudo-first-order kinetic model

The Lagergren pseudo first-order equation is a simple kinetic analysis of sorption in the following form

$$\ln(qe - qt) = \ln qe - k_1 t \quad \ldots\ldots\ldots\ldots\ldots\ldots \quad (33)$$

where q_e and q_t are the sorbed concentration of phosphate at equilibrium and at any time t, respectively and k_1 is the overall rate constant of first-order sorption. The slope of the plot of $\ln(q_e - q_t)$ as a function of t can be used to determine the first-order rate constant k_1.

In order to define the adsorption kinetics of phosphate, the kinetics parameters for the adsorption process were studied at pH=6, adsorbant dosage of 1 g/L, phosphate concentration (5-25 mg/L) with interval of 5 mg/L, contact times ranging from (20-120) min with 20 min interval and at room temperature. The PFO kinetic model was shown in Figure 17. As shown from the Figure 18 the sorption kinetics of phosphate by Fe_3O_4 NPs were not represented by pseudo first order kinetics model because of the theoretical qe value for the kinetic model doesn't match with the experimental qe values as indicated in Table 5.

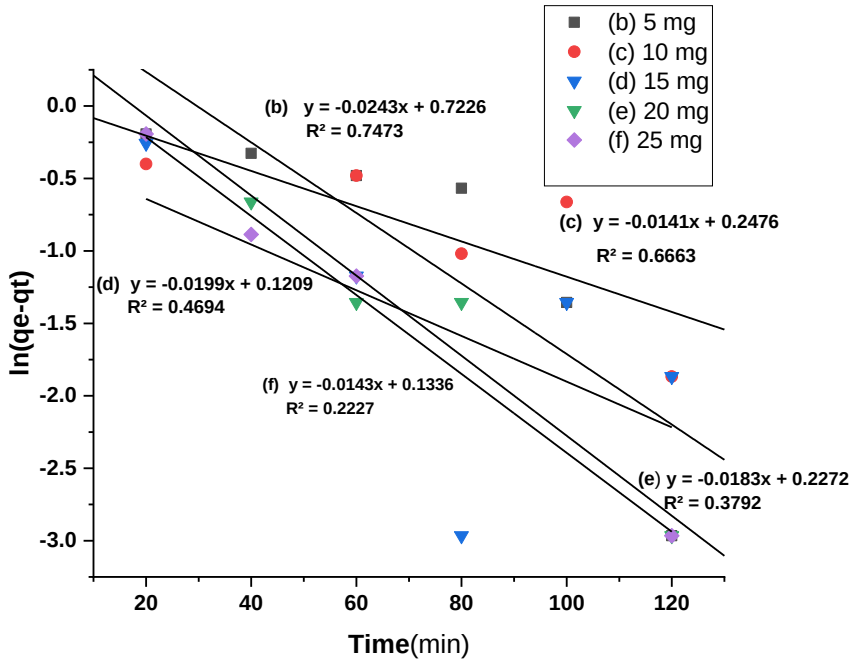

Figure 17: Pseudo-first-order plot for phosphate ion adsorption at different concentration

4.8.2 Pseudo-second-order kinetic model

Figure 18 shows the pseudo second order kinetics at different concentration (5 mg/L - 25 mg/L), pH=6 and adsorbant dosage of 1 g/L. As shown from the graph the experimental data for sorption kinetics of phosphate removal by Fe_3O_4 NPs were strongly fitted to pseudo second order kinetics model because the calculated and experimental phosphate removal were very close to each other as it can be seen from the Table 5.The q_e (cal) and rate constant was calculated from the slope and intercepts of the graph t/qt vs. t graph. As shown from the table the regression coefficient value i.e $R^2 \approx 1$, of pseudo second order kinetics greater than pseudo first order kinetics confirms that the adsorption obeys pseudo 2^{nd} order and the adsorption process is governed by chemisorption (Dong-Wan Cho, 2015). The pseudo-second order model can be expressed as follows:

$$t/q_t = \frac{1}{k_2 q_e^2} + \frac{t}{q_e} \text{..... (33)}$$

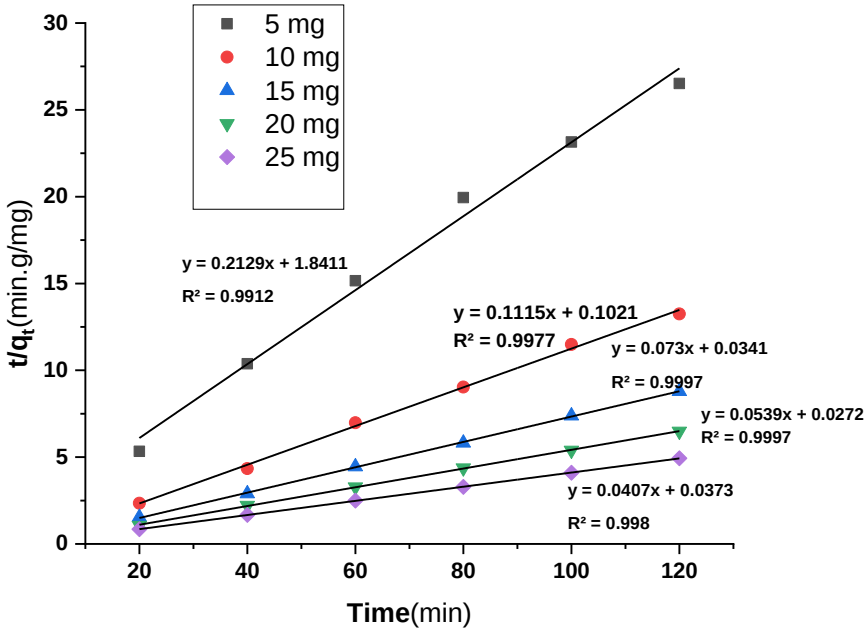

Figure 18: Pseudo-second-order plot for phosphate ion adsorption at different concentration

Table 5: Comparison between the adsorption rate constants, qe, and correlation coefficients associated with pseudo-first-order and to the pseudo-second-order rate equations

Intial phosphate Concentration (mg/L)	pseudo-first-order rate equation			pseudo-second-order rate equations		
	k_1 (min^{-1})	q_e (mg/g)	R^2	k_2 (g/mg min)	q_e (mg/g)	R^2
5	0.0243	2.059	0.0747	0.0246	4.69	0.9912
10	0.0141	1.28	0.66	0.122	8.96	0.997
15	0.0199	1.1285	0.46	0.156	13.69	0.997
20	0.0183	1.255	0.379	0.106	18.55	0.997
25	0.0143	1.1429	0.22	0.0447	24.57	0.998

4.9 Adsorption isotherms Study

The adsorption isotherm provides a relationship between the concentration of phosphate in solution and the amount of phosphate adsorbed on the solid phase when both phases are in equilibrium. The most widely used isotherm equations are Langmuir and Freundlich equations. These isotherms are useful for estimating the total amount of adsorbent needed to adsorb a required amount of adsorbate from solution. Isotherm studies were conducted by varying the initial phosphate concentration from 5 to 25 mg/L and maintaining the adsorbent dosage of 1 g for contact time of 120 min. The basic Langmuir model is based on two critical assumptions about the surface and the sorption process. First, all sorption sites on the surface are assumed to be identical i.e., they have equal binding strengths with a given sorbate. Second, only a monolayer of sorbate can be adsorbed to the solid; once all sites are occupied by sorbate molecules, no more sorption can occur (William, 2011). The Langmuir isotherm was applied for the sorption equilibrium on Fe_3O_4 according to the equation

$$C_e/q_e = \frac{1}{K_L Qe} + \frac{Ce}{Qe} \quad \text{..... (34)}$$

where Ce is the equilibrium concentration of phosphate in solution (mg/L), qe is the amount of solute sorbed per unit mass of EGLE coated Fe_3O_4 NPs at equilibrium (mg/g) and Qe (mg/g) and b (L/mg) are the Langmuir constants related to monolayer sorption capacity and free energy of sorption, respectively (O.I.M. Ali, 2011). Figure 19 shows Langmuir isotherm model for phosphate adsorption

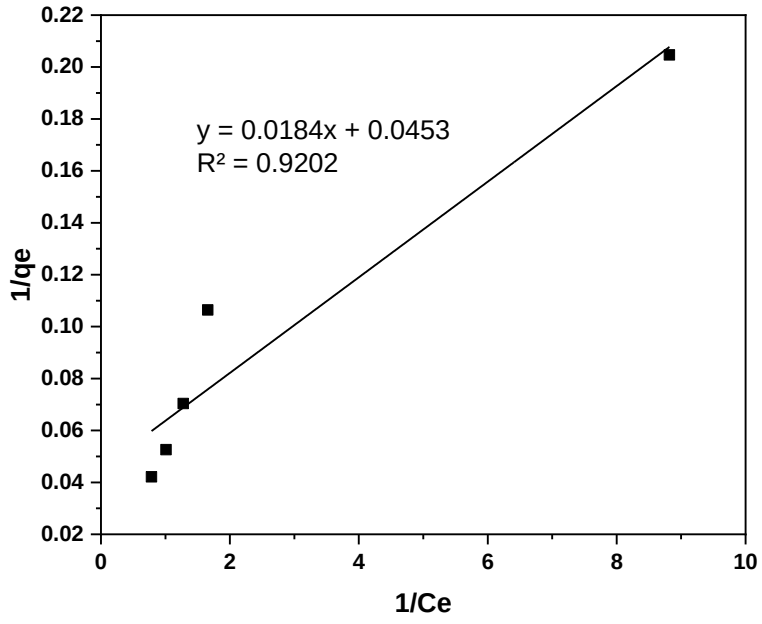

Figure 19: Langmuir isotherm model for phosphate ion adsorption

The shape of the Langmuir isotherm is identified with the dimensionless RL parameter

$$R_L = \frac{1}{1+K_L C_o} \ldots\ldots\ldots\ldots\ldots\ldots (35)$$

Where b is the Langmuir parameter (mg/g) and C_0 is the initial concentration of the solute (mg/L). The result depends on the shape of the isotherm: R= 0 indicates that the adsorption is irreversible, R= 1 linear, R > 1 unfavorable and 1 < R_L< 0 indicates that conditions are favorable for adsorption. From the graph we can calculate the R_L value which is greater than 0 but less than 1 indicating Langmuir isotherm is favorable (N.M Pooresmaeil, 2020). The maximum adsorption capacity (q_m) for Langmuir Isotherm model is 26.52 mg/g, K_L (Langmuir isotherm constant) is 2.47 L/mg and R_L (the separation factor) 0.075, 0.039, 0.026, 0.019, and 0.016 for 5, 10, 15, 20, and 25 mg/L of initial concentration respectively. This reflects that in all the cases, R_L values fall between 0 and 1, indicating favorable adsorption of phosphate and the R-Square value for the Isotherm model is 0.9202.

The simple Freundlich isotherm is often used for heterogeneous surface energy systems according to the equation:

$$\ln qe = \ln k + 1/n \ln Ce \ldots\ldots\ldots\ldots\ldots\ldots (36)$$

Where qe is the amount of solute sorbed per unit mass of EGLE coated Fe_3O_4 NPs at equilibrium (mg/g) and Ce is the equilibrium concentration of phosphate in solution (mg/L). K and n are constants characteristics of the system. ln k and 1/n are the Freundlich constants related to sorption capacity and sorption intensity of the sorbent, respectively. The isotherms based on the experimental data and the parameters obtained from linear regression of Freundlich isotherm model shown in Figure 20. For the Freundlich isotherm if 1/n (Freundlich parameter) is less than 1.0, the adsorption intensity is favorable over the entire range of the studied concentration. However, if 1/n is more than 1.0, the adsorption intensity is favorable at a higher concentration and much less at a lower concentration. By drawing the chart of Ln q_e versus Ln C_e the qe, K_F, n, and C_e can be determined (N.M Pooresmaeil, 2020).

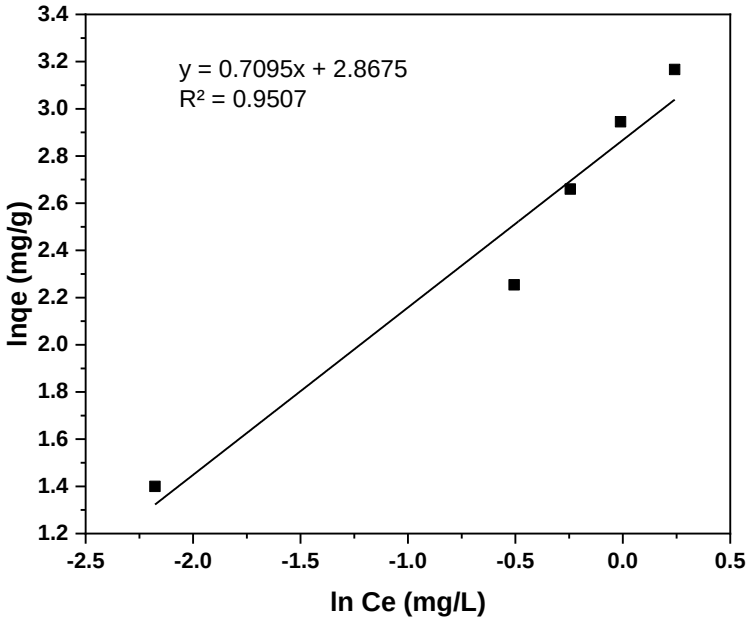

Figure 20: Freundlich isotherm model for phosphate ion adsorption

Based on the adsorption experimental data on Figure 21 the R^2 values of Freundlich isotherm models is greater than Langmuir isotherm model for biosynthesized Fe_3O_4 NPs as shown in table 6 which indicates that the Freundlich isotherm model is suitable for describing the adsorption phenomena of phosphate onto biosynthesized Fe_3O_4 NPs.

Table 6: Langmuir and Freundlich isoth0erm model constants and correlation coefficients for adsorption of phosphate

Adsorbent type	Isotherm	Regression (R^2)	Estimated isotherm parameters
Fe_3O_4	Langmuir	0.9202	K_L = 0.0379 L/mg q_m = 21.8 mg/g
	Freundlich	0.9507	$\frac{1}{n} = 0.709$, n = 1.41 $K_f = 17.60$

Table 7 presents a comparison of adsorption capacity of biosynthesized Fe_3O_4 with other various adsorbents for phosphate adsorption. Although the direct comparison is done using the adsorption capacity of EGLE coated Fe_3O_4 NPs via the Langmuir, q_0 value with other adsorbent materials. it was found Thus, these results indicate that biosynthesized Fe_3O_4 NPs has relatively high potential to be used as a commercial adsorbent for the removal and recovery of phosphate from aqueous solutions.

Table 7: Comparison of adsorption capacity of Fe_3O_4 adsorbant with other magnetic adsorbents

Adsorbent Type	Maximum adsorption capacity	Reference
EGLE Coated Fe_3O_4	21.8 mg/L	Current work
Phosphorous adsorption on synthesized magnetite in wastewater	15.2 mg/g	(Jeongyun Choi J. C.-O., 2016)
Removal of phosphate from aqueous solution by magnetic Fe–Zr binary oxide	13.65 mg/g	(Fei Long, 2011)
Magnetite for phosphorus removal in low concentration	0.158 mg/g	(Heng Xiang C. L., 2014)
Application of magnetic nano-particles for phosphorus removal	3.65 mg/g	(Yao-Jen Tu a, 2015)

4.10 Desorption Study

The Calibration curve for standard phosphate solution were done by at concentrations of (0.6 mg/L, 1 mg/L, 1.5 mg/L, 2 mg/L). A calibration curve of absorbance against phosphate concentrations was then plotted as shown in Figure 21.

Table 8: the calibration curve data for Desorption Study

Concentration of Standard(mg/L)	Absorbance
0.6	0.024
1	0.026
1.5	0.027
2	0.03

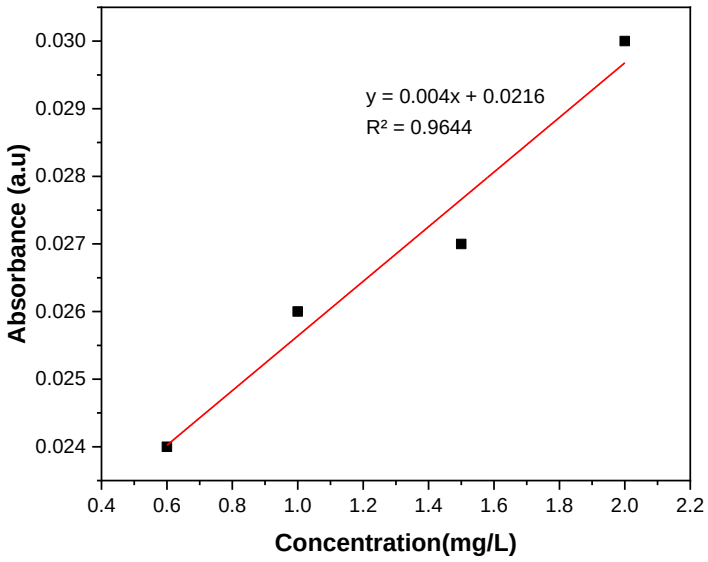

Figure 21: Calibration curve for Desorption Study

It has been reported that the solution pH can alter the desorption of phosphate from iron oxide based materials by changing the amount of charge and the charge characteristics of the phosphate and the surface of the materials and further changing the dominant adsorption/desorption mechanisms (Lei Hou Q. L., 2020). Acids and bases have been successfully used in removing both specific and nonspecific sorbed phosphate. This is because phosphate sorption decreases at pH below 3-4 and above 8-10. The reason for the reduction of phosphate sorption below pH 3-4 is that at low pH, phosphate is predominantly present as the unionised H_3PO_4 species that has very low sorption capacity. At pH > 8-10, both the sorbent and phosphate species in solution are highly negatively charged (HPO_4^{2-}, PO_4^{3-}), providing an unfavourable condition for sorption to the negatively charged sorbent. Furthermore, the increased number of OH^- ions present at high pH values competes with phosphate for sorption, thereby decreasing phosphate sorption. It is known that at high alkaline pH, $PO4^{3-}$ species are the predominant in the solution medium and the Fe_3O_4 is deprotonated and negatively charged, which is favorable for desorption of the adsorbed phosphate (Mengxue Li J. L., 2017).

The desorption study were done using 25 mg/L of phosphate solution in the pH ranges of 8-14 and contact time of 6 hour. High concentrations of acids and bases are not suitable for certain sorbents (oxides of Si, Fe, and AL; Carbonates of Ca and Mg) because they can dissolve or corrode parts of the sorbents or cause structural changes, leading to problems in regeneration and reuse of the sorbents (Khalid Z. Elwakeel, 2020). Desorption experiments were then performed using calcinated Fe_3O_4 prepared at 2:1 ratio to examine the reversibility of the sorption reaction. From the experiment it was observed that phosphate desorption rate was less than 20% up to pH 8-10, which indicated that phosphate adsorption on Fe_3O_4 was irreversible at this pH ranges; however, ≈ 45% of phosphate was desorbed at pH 11, and desorption rate was increased from pH 9-11 as shown in Figure 22.

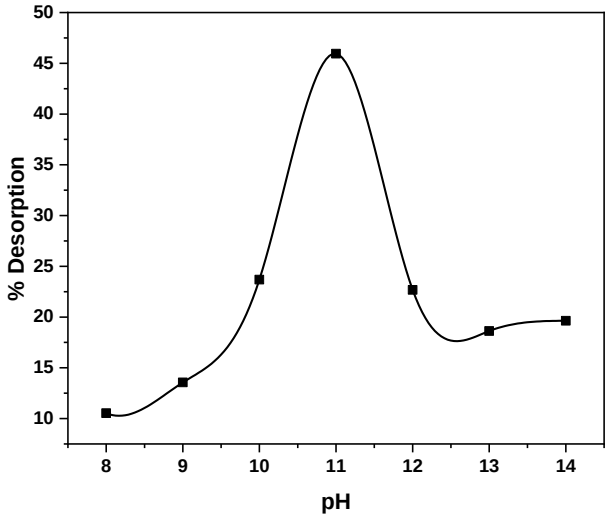

Figure 22: Desorption efficiency of phosphate adsorbed on Fe_3O_4 NPs.

CHAPTER FIVE

5. Conclusion and Recommendations

5.1. Conclusion

In this research work, an economical, environmentally friendly magnetic adsorbent has been applied to effectively separate phosphate from muncipal water system. Fe3O4 NPs were successfully prepared in copreciptation method using eucalyptus leaf extracts. Eucalyptus leaf extracts with high polyphenols content act as both reducing and capping agents for the nanoparticles. Furthermore, by changing the amount of the precursor material, the shape and size of the nanoparticles can be controlled which possesses benefits for synthesis process. The formation, structure, size, surface morphology, thermal stability, and sorption capacities of the synthesized Fe_3O_4 nanomaterials have been characterized by using different characterization techniques such as FTIR, XRD, SEM, TGA-DTA, DRS and UV-Vis analysis. The FTIR spectra spectra reveal that EGLE has been successfully coated onto surface of Fe_3O_4 by chemical bond. The result also showed that presence of EGLE uses to controls size, functionalities and prevents oxidation.

Adsorption study was carried by changing different parameters at different pH values, initial adsorbate concentrations, contact times, and adsorbent dosage. It was observed that the efficient removal of phosphate ions was achieved from neutral to acidic pH range, initial concentration (20 mg/l), adsorbent dosage 1.5 g/L and contact time of 120 minute. The adsorption isotherms and kinetics were investigated in detail at optimum PH.

The Adsorbton isotherms studies indicate that the adsorption of phosphate ion onto Fe_3O_4 surface was obeyed Freundlich isotherm model over all concentration range studied as compared to Langmuir isotherm, which shows heterogeneous adsorption process. The kinetic study revealed that adsorption process was well fitted the pseudo second order kinetic model. Based on observation of adsorption kinetics adsorption mainly occurs through chemisorption and thus indicative of strong bonding between phosphate and the adsorbent nanoparticles. All the above results show that the obtained Fe_3O_4 nanoparticles are excellent nano-adsorbents for decontamination of phosphate ion pollutants.

5.2 Recommendation

This research study used synthetic phosphate solution to avoid influence of any other Competitive substances on the adsorption process. Therefore, it is suggested to further evaluate the adsorption capability of the adsorbent by using effluents arising from municipal waste water. It is also possible to study the sorption thermodynamics of the system as well as desorption study to get a full picture of the removal capability of the biosynthesized Fe_3O_4 for removal of phosphate ions from different types of wastewater. Other studies should be conducted on the effectiveness of the biosynthesized Fe_3O_4 adsorbent in removal of essential nutrients like NH_3, NO_2^- and NO_3^-.

REFERENCES

1. Ahmad Abo Markeb, A. A. (2016). Phosphate removal and recovery from water using nanocomposite of immobilized magnetite nanoparticles on cationic polymer. *Environ Technol*, 1-15.

2. Aidin Lak, M. K. (2013). Size dependent structural and magnetic properties of FeO–Fe3O4 nanoparticles. *Nanoscale*, 12286–12295.

3. Alagumira Meyyappan, S. B. (2014). One Step Synthesis Of Iron Oxide Nanoparticles Via Chemical And Green Route An Effective Comparison. *International Journal of Pharmacy and Pharmaceutical Sciences*, 70-74.

4. Ali Othman, E. D. (2018). Nanoporous Sorbents for the Removal and Recovery of Phosphorus from Eutrophic Waters: Sustainability Challenges and Solutions. *ACS Sustainable Chem. Eng*, 1-20.

5. Ali, A. Z. (2016). Synthesis, characterization, applications, and challenges of iron oxide nanoparticles. *Nanotechnology, science and applications, 9*, 49–67.

6. András E.Vladára, V.-D. H. (2020). Characterization of nanoparticles by scanning electron microscopy. In W. Unger, *Characterization of Nanoparticles: Measurement Processes for Nanoparticles* (pp. 7-27). Elsevier.

7. Ashok Bankar, G. N. (2018). Recent Trends in Biosorption of Heavy Metals by Actinobacteria. *New and Future Developments in Microbial Biotechnology and Bioengineering*, 257-275.

8. Attarad Ali, 1. H. (2016). Synthesis, characterization, applications, and challenges of iron oxide nanoparticles. *Nanotechnol Sci Appl*, 49–67.

9. Augustine Amalraj, A. P. (2017). Removal of fluoride from drinking water using aluminum hydroxide coated activated carbon prepared from bark of Morinda tinctoria. *Appl Water Sci (2017) 7*, 2653–2665.

10. Azza M. Mazrouaa, M. G. (2019). Physical and magnetic properties of iron oxide nanoparticles with a different molar ratio of ferrous and ferric. *Egyptian Journal of Petroleum 28* , 165–171.

11. B. Xing, J. P. (2005). SORPTION/Organic Chemicals. In D. Hillel, *Encyclopedia of Soils in the Environment* (p. Encyclopedia of Soils in the Environment). Academic Press.

12. Balasuriya, A. (2018). Coastal Area Management: Biodiversity and Ecological Sustainability in Sri Lankan Perspective. In A. V. (s): Chandrakasan Sivaperuman, *Biodiversity and Climate Change Adaptation in Tropical Islands* (pp. 701-724). Academic Press.

13. Bauer, N. T. (2020). Physical and chemical properties of nanomaterials. In V. V. Sarita P. Patil, *Nanomedicines for Breast Cancer Theranostics* (pp. 17-31). Elsevier.

14. Bergquist, C. (2011). Phosphorous recovery from iron (III) phosphate. In *Approaches to Recover Phosphorous* (p. 27). MSc Thesis Submitted to University of Chalmers University of Technology.

15. Bhatnagar, A. (2012). Iron Oxide Nanoadsorbents for Removal of Various Pollutants from Wastewater: An Overview. In N. N. Nassar, *Application of Adsorbents for Water Pollution Control* (pp. 81-118). Bentham Science Publishers.

16. Bhattacharyya, N. K. (2016). Nanometal Oxide Adsorbents for the Remediation of Heavy Metals in Water. In A. K. Mishra, *Nanomaterials for Water Remediation: Inorganic Oxide Materials* (pp. 26-43). Shrewsbury,UK: Smithers Rapra Technology Ltd.

17. Blaney, L. (2007). Magnetite (Fe3O4): Properties, Synthesis, and Applications. *Lehigh Review*, 35-40.

18. Boris I. Kharisov, H. V.-P. (2012). Iron-containing nanomaterials: synthesis, properties, and environmental applications. *The Royal Society of Chemistry* , 9325–9358.

19. Boyd, C. E. (2015). Water Quality:An Introduction. In *Phosphorus* (pp. 244-248). New York: Springer International Publishing.

20. Daoush, W. M. (2017). Co-Precipitation and Magnetic Properties of Magnetite Nanoparticles for Potential Biomedical Applications. *Journal of Nanomedicine Research*, 1-2.

21. Dekun Hou, J. H. (2013). Effects of Environmental Factors on Nutrients Release at Sediment-Water Interface and Assessment of Trophic Status for a Typical Shallow Lake, Northwest China. *The Scientific World Journal*, 1-8.

22. Derek Fawcett, J. J. (2017). A Review of Current Research into the Biogenic Synthesis of Metal and Metal Oxide Nanoparticles via Marine Algae and Seagrasses. *Journal of Nanoscience* , 1-3.

23. Derya Aksu Demirezen, Y. S. (2019). Green synthesis and characterization of iron oxide nanoparticles using Ficus carica (common fig) dried fruit extract. *Journal of Bioscience and Bioengineering VOL. 127 No. 2*, 241-245.

24. Dimitris Dermatas, T. M. (2018). Adsorption of Groundwater Pollutants. In N. Q. Marta I. Litter, *Iron Nanomaterials for Water and Soil Treatment* (pp. 41-43). Singapore: Pan Stanford Publishing Pte. Ltd.

25. Dong-Wan Cho, B.-H. J.-M. (2015). Magnetic chitosan composite for adsorption of cationic and anionic dyes in aqueous solution. *Journal of Industrial and Engineering Chemistry*, 1-7.

26. Ekain Cagigal, M. O.-V. (2018). Environmental Effects of the Application of Iron Nanoparticles for Site Remediation. In N. Q. Marta I. Litter, *Iron Nanomaterials for Water and Soil Treatment* (pp. 283-299). 8 Temasek Boulevard Singapore : Pan Stanford Publishing Pte. Ltd.

27. Fei Long, J.-L. G.-M.-Y.-H. (2011). Removal of phosphate from aqueous solution by magnetic Fe–Zr binary oxide. *Chemical Engineering Journal*, 1-8.

28. George William Kajjumba, S. E. (2018). Modelling of Adsorption Kinetic Processes—Errors, Theory and Application. In S. Edebali, *Advanced Sorption Process Applications* (pp. 1-20). Selçuk University, Turkey: Intech Open publisher.

29. Getaneh Diress Gesesse, A. G.-B.-F. (2020). On the analysis of diffuse reflectance measurements to estimate the optical properties of amorphous porous carbons and semiconductor/carbon catalysts. *Journal of Photochemistry & Photobiology A: Chemistry 398*, 1-10.

30. Gray, N. F. (2010). An Introduction for Environmental Scientists and Engineers. In *Nutrient Removal* (pp. 553-558). China: Elsevier Ltd.

31. Grégorio Crini, E. L. (2019). Advantages and disadvantages of techniques used for wastewater treatment. *Environmental Chemistry Letters, Springer Verlag*, 17 (1), pp.145-155.

32. H.Pandaa, N. (2017). Studies on adsorption behavior of an industrial waste for removal of chromium from aqueous solution. *South African Journal of Chemical Engineering*, 132-138.

33. Haddad, M. T. (2017). Antimicrobial Applications of Superparamagnetic Iron Oxide Nanoparticles:Perspectives and Challenges. In A. M. Anton Ficai, *Nanostructures for Antimicrobial Therapy* (pp. 531-550). Elsevier.

34. Hasfalina Che Man, W. H. (2012). Adsorption Potential of Unmodified Rice Husk For Boron Removal. *Bioresources*, 1-13.

35. Hayton, J. (2018). Characteristics and Behavior of Nanoparticles and Its Dispersion Systems. In H. Kamiya, *Nanoparticle Technology Handbook* (pp. 13-135). AE Amsterdam, Netherlands: Elsevier.

36. Helmut Kroiss, H. R. (2011). Phosphorus in Water Quality and Waste Management. In S. Kuma, *Integrated Waste Management: Volume II* (pp. 184-206). Rijeka,Croatial: In Tech.

37. Henam Sylvia Devi, M. A. (2017). Green synthesis of iron oxide nanoparticles using Platanus orientalis leaf extract for antifungal activity. *Green Process Synth*, 1-8.

38. Heng Xiang, C. L. (2014). Magnetite for phosphorus removal in low concentration phosphorus-contained water body. *Advances in Environmental Research, Vol. 3, No. 2* , 163-172.

39. Heng Xiang, C. L. (2014). Magnetite for phosphorus removal in low concentration phosphorus-contained water body. *Advances in Environmental Research Vol. 3 No. 2*, 163-172.

40. Ifelebuegu, U. A. (2020). Kinetics, Isotherms, and Thermodynamic Modeling of the Adsorption of Phosphates from Model Wastewater Using Recycled Brick Waste. *processes*, 1-15.

41. Igwebike-Ossi, C. D. (2017). X-Ray Techniques. In A. Ali, *Failure Analysis and Prevention* (pp. 166-170). IntechOpen.

42. Imran Ali, C. P. (2019). Water Purification Using Magnetic Nanomaterials. In K. A.-E. Mohamed, *Magnetic Nanostructures Environmental and Agricultural Applications,Ram Prasad* (pp. 162-164). Switzerland: Springer Nature Publisher.

43. Iravani, H. K. (2012). Silver Nanoparticles. In A. A. Hashim, *The Delivery of Nanoparticles* (pp. 1-7). Janeza Trdine 9, 51000 Rijeka, Croatia: InTech.

44. Ivar, U. (2013). Phosphorus recovery from municipal wastewater - Literature Review. 11-18.

45. Jaison Jeevanandam, Y. S. (2018). Aqueous Eucalyptus globulus leaf extract-mediated biosynthesis of MgO nanorods. *Applied Biological Chemistry*, 197–208.

46. Jayanta Kumar, K.-H. B. (2014). Green Nanobiotechnology: Factors Affecting Synthesis and Characterization Techniques. *Hindawi Publishing Corporation*, 1-13.

47. Jeongyun Choi, J. C. (2016). Phosphorous adsorption on synthesized magnetite in wastewater. *Journal of Industrial and Engineering Chemistry 34*, 198-203.

48. Jeongyun Choi, J. C.-O. (2016). Phosphorous adsorption on synthesized magnetite in wastewater. *Journal of Industrial and Engineering Chemistry*, 1-6.

49. Jeongyun Choi, J. C.-O. (2016). Phosphorous adsorption on synthesized magnetite in wastewater. *Journal of Industrial and Engineering Chemistry 34*, 198-203.

50. Jianlong Wang, X. G. (2020). Adsorption isotherm models: Classification, physical meaning,application and solving method. *Chemosphere 258 127279*, 3-22.

51. Jonas Bayuo, M. A.-B. (2020). Desorption of chromium (VI) and lead (II) ions and regeneration of the exhausted adsorbent. *Applied Water Science*, 1-6.

52. Jose Torrent, V. B. (2002). DIFFUSE REFLECTANCE SPECTROSCOPY OF IRON OXIDES. *Encyclopedia of Surface and Colloid Science*, 1440-1446.

53. Joshua T. Bunce, E. N. (2018). A Review of Phosphorus Removal Technologies and Their Applicability to Small-Scale Domestic Wastewater Treatment Systems. *Frontiers in Environmental Science*, 2-5.

54. K. Sairam Goud, K. U. (2017). Magnetic Iron Oxide Nanoparticles: Various PreparationMethods and Properties. *Journal of Scientific Research in Science, Engineering and Technology*, 1-4.

55. Keno David Kowanga*, E. G. (2016). Kinetic, sorption isotherms, pseudo-first-order model and pseudo-second-order model studies of Cu(II) and Pb(II) using defatted Moringa oleifera seed powder. *The Journal of Phytopharmacology*, 71-78.

56. Khadeeja Parveen, V. B. (2016). Green synthesis of nanoparticles: Their advantages and disadvantages. *Journal of Applied Physics*, 1-8.

57. Khalid Z. Elwakeel, A. M. (2020). Perspectives regarding metal/mineral-incorporating materials for water purification: with special focus on Cr(VI) removal. *Materials Advances*, 1-29.

58. Khan.S., I. M. (2013). Evaluation of Coal as Adsorbent for Phosphate Removal. *Arab. J. Geosci*, 1113–1117.

59. Kleemann, R. (2015). *Sustainable Phosphorus Recovery from Waste.*

60. Lee, B. (2007). Magnetite (Fe3O4): Properties, Synthesis, and Applications. *Lehigh Review at Lehigh Preserv*, 30-40.

61. Lei Hou, Q. L. (2020). Mechanisms that control the adsorption desorption behavior of phosphate on magnetite nanoparticles: the role of particle size and surface chemistry characteristics. *RSC Advances*, 1-11.

62. Lei Hou, Q. L. (2020). Mechanisms that control the adsorption–desorption behavior of phosphate on magnetite nanoparticles: the role of particle size and surface chemistry characteristics. *RSC Advances*, 2378-2388.

63. Loganathan, S. V. (2013). Removal and recovery of phosphate from water using sorption. *Critical Reviews in Environmental Science and Technology*, 1-5.

64. Lokesh Srinath Ganapathe, M. A. (2019). Magnetite (Fe3O4) Nanoparticles in Biomedical Application: From Synthesis to Surface Functionalisation. *Journal of Magnetochemistry*, 1-5.

65. M. Nurbasa, H. G. (2017). Extract, An Eco-Friendly Approach to Synthesis and Characterization of Magnetite (Fe3o4) Nanoparticles Using Platanus Orientalis L. Leaf. *Digest Journal of Nanomaterials and Biostructures*, 993 -1000.

66. M. Padervanda, M. V. (2014). Experimental and Theoretical Study on the Structure and Photoactivity of XFe2O4 (X = Mn, Fe, Ni, Co, and Zn) Structures. *Russian Journal of Physical Chemistry,Vol. 88, No. 13,*, 2451–2461.

67. M. Ruthiraan, N. M. (2019). An Overview of Magnetic Material:Preparation and Adsorption Removal of Heavy Metals from Wastewater. In M. A. Kamel A. Abd-Elsalam, *Nanotechnology in the Life Sciences* (pp. 132-144). Springer Nature Switzerland.

68. M. T. Hossain1, M. M. (2018). Magnetite (Fe3O4) nanoparticles for chromium removal. *Bangladesh J. Sci. Ind. Res.53(3),*, 219-224.

69. Mackenzie L. Davis, S. J. (2014). Water Treatment. In S. J. Mackenzie L. Davis, *Principles of Environmental Engineering and Science* (pp. 481-485). New York, NY 10020: McGraw-Hill.

70. Madan Singha, M. G. (2018). Size and shape effects on the band gap of semiconductor compound nanomaterials. *Journal of Taibah University for Science*, 1-7.

71. Mahapatra, A. (2015). *Fabrication And Characterization Of Novel Iron Oxide/ Alumina Nanomaterials For Environmental Applications.* Thesis submitted to National Institute of Technology, Rourkela, India in partial fulfillment of the requirements for the degree of Doctor of Philosophy.

72. Malihe Pooresmaeil, H. N. (2020). Chapter 14 - Application of polysaccharide-based hydrogels for water treatments. In Y. Chen, *Hydrogels Based on Natural Polymers* (pp. 411-455). Elsevier.

73. Mamun Rashid, N. T. (2017). Effective removal of phosphate from aqueous solution using humic. *Water Research 123 353-360,* 1-8.

74. Mamun Rashid, N. T. (2017). Effective removal of phosphate from aqueous solution using humic acid coated magnetite nanoparticles. *Water Research 123 (2017),* 353-360.

75. Manahan, S. (2017). Water Chemistry: Green Science and Technology. In S. Manahan, *Phosphorus Removal* (pp. 195-196). London: CRC Press is an imprint of the.

76. Marluce Oliveira da Guarda Souza, M. V. (2020). Production and in situ transformation of hematite into magnetite from the thermal decomposition of iron nitrate or goethite mixed with biomass. *Journal of Thermal Analysis and Calorimetry*, 1-9.

77. Mate William D. CallisterJR, D. G. (2018). The Structure of Crystalline Solids. In D. G. Mate William D. CallisterJR, *Materials Science and Engineering an Introduction* (pp. 84-85). River Street,Hoboken: John Wiley & Sons Publisher.

78. Mbaeze MC, A. V. (2017). Comparative Assessment of Performance of Aluminium Sulphate (Alum) and Ferrous Sulphate as Coagulants in Water Treatment. *Modern Chemistry & Applications*, 1-5.

79. Mengxue Li, J. L. (2016). Phosphate adsorption on metal oxides and metal hydroxides: A comparative review. *Environmental Reviews Volume 24, Number 3*, 12-20.

80. Mengxue Li, J. L. (2016). Phosphate adsorption on metal oxides and metal hydroxides:A comparative review. *Environ. Rev. 24*, 319–332.

81. Mengxue Li, J. L. (2017). Phosphate adsorption on metal oxides and metal hydroxides:A comparative review. *Environ. Rev. 24*, 319–332.

82. Metcalf & Eddy, I. a. (2014). *Wastewater Engineering: Treatment and Resource Recovery 5th Edition.* New York: McGraw Hill Education.

83. Mohammad A. Al-Ghouti, D. A. (2020). Guidelines for the use and interpretation of adsorption isotherm models: A review. *Journal of Hazardous Materials Volume 393*.

84. Motlagh, R. G. (2014). Biological Phosphorus Removal. In S. Ahuja, *Comprehensive Water Quality and Purification* (pp. 150-160). 225 Wyman Street, Waltham, MA 02451, USA: Elsevier Inc.

85. N. Yeddou Mezenner, A. B. (2010). Kinetics and thermodynamic study of phosphate adsorption on iron hydroxide-eggshell waste. *Chemical Engineering Journal*, 1-7.

86. N.M Pooresmaeil, H. (2020). Application of polysaccharide-based hydrogels for water treatments. In Y. Chen, *Hydrogels Based on Natural Polymers* (pp. 411-445). Amsterdam, Netherlands: Elsevier.

87. Namazi, M. P. (2020). Application of polysaccharide-based hydrogels for water treatments. In Y. Chen, *Hydrogels Based on Natural Polymers* (pp. 411-444). Amsterdam, Netherlands: Elsevier publications.

88. Narayanaswamy, V., Sambasivam, S., Saj, A., Alaabed, S., Issa, B., Al-Omari, I., et al. (2021). Role of Magnetite Nanoparticles Size Molecules and Concentration on Hyperthermia under Various Field Frequencies and Strengths. *Molecules*, 26, 796.

89. Narendra Kumar, S. K. (2016). Essentials In Nanoscience And Nanotechnology. In *Characterization Tools for Nanomaterial's* (pp. 134-137). New Jersey: John Wiley & Sons.

90. Nene Ajinkya, X. Y. (2020). Magnetic Iron Oxide Nanoparticle (IONP) Synthesis to Applications: Present and Future. *Materials Review*, 14-17.

91. NuchareeNucharee Chomchoey, D. B. (2018). Effect of Calcination Temperature on the Magnetic Characteristics of Synthetic Iron Oxide Magnetic Nanoparticles for Arsenic Adsorption. *Chiang Mai J. Sci*, 1-13.

92. O.I.M. Ali, H. O. (2011). The removal of some rare earth elements from their aqueous solutions on by-pass cement dust (BCD). *Journal of Hazardous Materials*, 62-67.

93. O'Boyle, W. T. (2018). *Water Quality in 2017: An Indicators Report.* Wexford,Ireland: ENVIRONMENTAL PROTECTION AGENCY, IRELAND.

94. Oisik Das, N. K. (2019). The flammability of biocomposites. In F.-R. C. Durability and Life Prediction in Biocomposites, *Durability and Life Prediction in Biocomposites, Fibre-Reinforced Composites and Hybrid Composites* (pp. 335-365). Woodhead Publishing.

95. Olga Ruzhitskaya, E. G. (2017). Methods for Removing of Phosphates from Wastewater. *MATEC Web of Conferences 106, 07006,SPbWOSCE-2016*, 106.

96. Qi Li1, P. W. (2014). Nanostructured Visible-Light Photocatalysts for Water Purification. In R. S. Anita Street, *Nanostructured Visible-Light Photocatalysts for Water Purification* (pp. 297-313). Kidlington, Oxford: Elsevier.

97. R.B. Shrivastava, P. S. (2014). Polysaccharide-Based Nanosorbents in Water Remediation. In A. K. Mishra, *Application of Nanotechnology in Water Research* (pp. 79-107). New Jersey,USA: John Wiley & Sons.

98. Raja Das, C. W.-T.-H. (2019). Magnetic Vortex and Hyperthermia Suppression in Multigrain Iron Oxide Nanorings. *Appl. Sci*, 1-11.

99. Rashed, M. (2013). Adsorption Technique for the Removal of Organic Pollutants from Water and Wastewater. *InTechOpen*, 1-28.

100. Ravindra Kumar Gautam, M. C. (2016). Nanotechnology for Water Cleanup. In M. C. Ravindra Kumar Gautam, *Nanomaterials for Wastewater Remediation* (pp. 10-12). The Boulevard, Langford Lane, Kidlington, Oxford OX5 1GB, UK: Butterworth-Heinemann.

101. Robert Ianos, E.-A. T. (2018). g-Fe2O3 nanoparticles prepared by combustion synthesis, followed by chemical oxidation of residual carbon with H2O2. *Materials Chemistry and Physic*, 1-7.

102. Ruixi Bai, Y. Z. (2017). Rapid and highly selective removal of lead in simulated wastewater of rare-earth industry using diglycolamic-acid functionalized magnetic chitosan adsorbents. *Journal of Industrial and Engineering*, 1-43.

103. Ruttenberg, K. (2001). Phosphorus Cycle. *Encyclopedia of Ocean Sciences*, 2149-2162.

104. Sagadevan S, K. P. (2015). Analysis of Structure, Surface Morphology, Optical and Electrical Properties of Copper Nanoparticles. *J Nanomed Res 2(5)*, 1-5.

105. Saidur Rahman Chowdhury, E. K. (2010). Arsenic and chromium removal by mixed magnetiteemaghemite nanoparticles and the effect of phosphate on removal. *Journal of Environmental Management*, 1-10.

106. Shraddha Chauhan, L. S. (2019). Biosynthesis of iron oxide nanoparticles using plant derivatives of Lawsonia inermis (Henna) and its surface modification for biomedical application. *Nanotechnology for Environmental Engineering*, 1-10.

107. Sidra Iftekhar, D. L. (2018). Understanding the factors affecting the adsorption of Lanthanum using different adsorbents: A critical review. *Chemosphere 204* , 413-430.

108. Sinha Ray, R. G. (2020). Effect of reaction parameters on the adsorption. In R. G. Suprakas Sinha Ray, *In Micro and Nano Technologies,Carbon Nanomaterial-Based Adsorbents for Water Purification* (pp. 119-135). Elsevier.

109. Sirajunnisa Abdul Razack, A. S. (2019). Green synthesis of iron oxide nanoparticles using Hibiscus rosa-sinensis for fortifying wheat biscuits. *SN Applied Sciences* , 1-9.

110. Stefanos Mourdikoudis, R. M. (2018). Characterization techniques for nanoparticles:comparison and complementarity upon studying nanoparticle properties. *Nanoscale*, 12871–12934 .

111. Stepan, L. (2015). *The removal of residual concentrations of phosphorus from wastewater by means of coagulation and flotation.* Master's Thesis University of Oulu Faculty of Technology.

112. Suprakas SinhaRay, R. (2020). Effect of reaction parameters on the adsorption. In R. G. Suprakas Sinha Ray, *Carbon Nanomaterial-Based Adsorbents for Water Purification Fundamentals and Applications* (pp. 119-135). Elsevier .

113. Taylor, L. N. (2018). Phosphorus Eutrophication and Mitigation Strategies. In T. Zhang, *Phosphorus - Recovery and Recycling.* intechopen.

114. Ting Wang, X. J. (2014). Green synthesis of Fe nanoparticles using eucalyptus leaf extracts for treatment of eutrophic wastewater. *Science of the Total Environment*, 466–467 .

115. Toda, K. (2018). Optical Properties. In T. Y. Makio Naito, *Nanoparticle Technology Handbook* (pp. 338-354). Radarweg 29, PO Box 211, 1000 AE Amsterdam, Netherlands: Elsevier B.V. All rights reserved.

116. V.N. de Jonge, M. Elliott. (2013). Reference Module in Earth Systems and Environmental Sciences Encyclopedia of Inland Waters. In *Eutrophication* (pp. 61-73). Lawrence, KS, USA: Academic Press.

117. W.Zhang. (2014). Nanoparticle aggregation: principles and modeling. *Advances in experimental medicine and biology*, 19-43.

118. Walid, M. (2017). Co-Precipitation and Magnetic Properties of Magnetite Nanoparticles for Potential Biomedical Applications. *Journal of Nanomedicine Research*, 1-6.

119. Walker, F. (2014). Best Mangement practice for phosphorus in the enviroment.

120. Wei Wu, Q. H. (2008). Magnetic Iron Oxide Nanoparticles: Synthesis and Surface Functionalization Strategies. *Nanoscale Research Letters volume* , 2-4.

121. William Nivens, P. H. (2018). 4500-P PHOSPHORUS. In A. D. Rodger B. Bair, *Standard Methods of Water Analysis* (pp. 4-156). Washington, DC, New York: American Public Health Association.

122. William, P. L. (2011). An Introduction to Surface Chemistry and SorptionChemistry and Sorption. In P. L. Arnold, *An Introduction to the Chemistry of Natural and Engineered Aquatic Systems* (pp. 525-540). Madison Avenue, New York, New York: Oxford University Press.

123. Yao-Jen Tu a, b. C.-F.-K.-H. (2015). Application of magnetic nano-particles for phosphorus removal in aqueous solution. *Journal of the Taiwan Institute of Chemical Engineers 46*, 148-154.

124. Yao-Jen Tu, C.-F. Y. (2015). Application of magnetic nano-particles for phosphorus removal/recovery in aqueous solution. *Journal of the Taiwan Institute of Chemical Engineers*, 1-3.

125. YaserDahman. (2017). Nanopolymers. *Nanotechnology and Functional Materials for Engineers*, 121-144.

126. Yen Pin Yew, K. S. (2018). Green biosynthesis of superparamagnetic magnetite Fe3O4 nanoparticles and biomedical applications in targeted anticancer drug delivery system: A review. *Arabian Journal of Chemistry*, 1-5.

127. Zahra Sabouri, A. A. (2021). Green-based bio-synthesis of nickel oxide nanoparticles in Arabic gum and examination of their cytotoxicity, photocatalytic and antibacterial effects. *Green Chemistry Letters and Reviews*, 1-14.

APPENDIX

Table 9: The result of the effect of pH adsorption for different adsorbent

pH	[PO_4^{3-}] mg/L	Absorbance(2:1) (470 nm)	Absorbance (1:2) (470 nm)	Absorbance (1:1) (470 nm)	R.Con (2:1) mg/L	R.Con (1:2) mg/L	R.Coc (1:1) mg/L	%Rem (2:1)	%Rem (1:2)	%Rem (1:1)
1	25	0.041	0.047	0.051	0.99	1.266	1.449	96.036	94.935	94.201
2	25	0.04	0.043	0.045	0.944	1.0825	1.1743	96.22	95.669	95.302
3	25	0.02	0.034	0.032	0.027523	0.6697	0.577	99.889	97.321	97.68
4	25	0.021	0.039	0.027	0.073394	0.899083	0.348624	99.70642	96.40367	98.605
5	25	0.027	0.035	0.029	0.348	0.715	0.440367	98.6055	97.13761	98.238
6	25	0.025	0.034	0.033	0.256881	0.669725	0.623853	98.97248	97.3211	97.504
8	25	0.054	0.055	0.056	1.587156	1.633028	1.678899	93.65138	93.46789	93.284
10	25	0.048	0.047	0.049	1.311	1.266055	1.357	94.75	94.93	94.568
12	25	0.088	0.09	0.095	3.146789	3.238532	3.46789	87.41284	87.04587	86.12844
14	25	0.093	0.096	0.097	3.376147	3.513761	3.559633	86.49541	85.94495	85.76147

Table 10: Effect of adsorbent dose

Dos(g)	Absor1 (470 nm)	Absorb2 (470 nm)	Avg (470 nm)	Residual mg/L	% Remov
0.25	0.065	0.051	0.058	1.865979381	92.53608247
0.5	0.063	0.045	0.054	1.659793814	93.36082474
1	0.044	0.041	0.0425	1.067010309	95.73195876
1.5	0.049	0.031	0.04	0.93814433	96.24742268

Table 11: Effect of initial concentration

[P] in mg/L	Absorb 1 (470 nm)	Absorb 2 (470 nm)	Avg Absorb (470 nm)	Conc(Ce) (mg/L)	% Removal
5	0.024	0.024	0.024	0.113402062	97.73195876
10	0.038	0.029	0.0335	0.603092784	93.96907216
15	0.041	0.033	0.037	0.783505155	94.7766323
20	0.045	0.037	0.041	0.989690722	95.05154639
25	0.052	0.041	0.0465	1.273195876	94.90721649

Table 12: Effect of contact time

Contact Time (min)	Absor1 (nm)	Absrb 2 (nm)	Avg Absb (nm)	Residual Concent (nm)	% Removal
20	0.069	0.031	0.05	1.453608247	94.18556701
40	0.062	0.022	0.042	1.041237113	95.83505155
60	0.049	0.021	0.035	0.680412371	97.27835052
80	0.046	0.021	0.0335	0.603092784	97.58762887
100	0.044	0.024	0.034	0.628865979	97.48453608
120	0.046	0.018	0.032	0.525773196	97.89690722

Table 13: Result of Adsorption kinetics experiment at different Concentration

Dosage (mg)	t (min)	Absorbance (470 nm)	R.Concent	% Removal	q_t (mg/g)	q_e (mg/g)	q_e-q_t	ln(q_e-q_t)	t/q_t
5	20	0.046	1.247	75.051	3.752	4.525	0.773	-0.257	5.329
5	40	0.044	1.144	77.113	3.855	4.525	0.670	-0.400	10.374
5	60	0.042	1.041	79.175	3.958	4.525	0.567	-0.567	15.156
5	80	0.041	0.989	80.206	4.010	4.525	0.515	-0.662	19.948
5	100	0.035	0.680	86.391	4.319	4.525	0.206	-1.578	23.150
5	120	0.031	0.474	90.515	4.525	4.525	0	#NUM!	26.514
10	20	0.05	1.453	85.463	8.546	9.216494845	0.670103093	-0.400323709	2.340168878
10	40	0.037	0.783	92.164	9.216	9.216494845	0	#NUM!	4.340044743
10	60	0.049	1.402	85.979	8.597	9.216494845	0.618556701	-0.480366416	6.978417266
10	80	0.044	1.144	88.556	8.855	9.216494845	0.360824742	-1.019362917	9.033760186
10	100	0.047	1.298	87.010	8.701	9.216494845	0.515463918	-0.662687973	11.492891
10	120	0.04	0.938	90.618	9.061	9.216494845	0.154639175	-1.866660777	13.242320822
10	20	0.05	1.453	85.463	8.546	9.216494845	0.670103093	-0.400323709	2.340168878

[P] (mg/L)	t (min)	Absorbance (470 nm)	R.Conc (mg/L)	% Removal	q_t (mg/g)	q_e (mg/g)	q_e-q_t	ln(q_e-q_t)	t/q_t
15	20	0.06	1.969	86.872	13.030	13.804	0.773	-0.257	1.534
15	40	0.045	1.195	92.027	13.804	13.804	0	#NUM!	2.897
15	60	0.051	1.505	89.965	13.494	13.804	0.309	-1.173	4.446
15	80	0.046	1.247	91.683	13.752	13.804	0.051	-2.965	5.817
15	100	0.05	1.453	90.309	13.546	13.804	0.257	-1.355	7.382
15	120	0.048	1.350	90.996	13.649	13.804	0.154	-1.866	8.791
20	20	0.044	1.144	94.278	18.855	18.546	-0.309	#NUM!	1.060
20	40	0.06	1.969	90.154	18.030	18.546	0.515	-0.662	2.218
20	60	0.055	1.711	91.443	18.288	18.546	0.257	-1.355	3.280
20	80	0.055	1.711	91.443	18.288	18.546	0.257	-1.355	4.374
20	100	0.05	1.453	92.731	18.546	18.546	0	#NUM!	5.391
20	120	0.051	1.505	92.474	18.494	18.546	0.0515	-2.965	6.488
20	20	0.044	1.144	94.278	18.855	18.546	-0.309	#NUM!	1.060
25	20	0.05	1.453	94.185	23.546	24.371	0.824	-0.192	0.849
25	40	0.042	1.041	95.835	23.958	24.371	0.412	-0.885	1.669
25	60	0.04	0.938	96.247	24.061	24.371	0.309	-1.173	2.493
25	80	0.034	0.628	97.484	24.371	24.371	0	#NUM!	3.282
25	100	0.034	0.628	97.484	24.371	24.371	0	#NUM!	4.103
25	120	0.035	0.680	97.278	24.319	24.371	0.0515	-2.965	4.934

Table 14: Results for isotherm models at different concentrations

[P] (mg/L)	5	10	15	20	25
Absorb 1(nm)	0.024	0.038	0.041	0.045	0.052
Absorb 2(nm)	0.024	0.029	0.033	0.037	0.041
Avg Absorb(nm)	0.024	0.0335	0.037	0.041	0.0465
Conc(Ce)(mg/L)	0.113	0.603	0.783	0.989	1.273
1/Ce (mg/L)	8.818	1.658	1.276	1.01	0.785
ln Ce	-2.176	-0.505	-0.243	-0.01	0.241
% Removal	97.731	93.969	94.776	95.051	94.907
qe (mg/g)	4.886	9.396	14.216	19.01	23.726
lnqe	1.4	2.254	2.659	2.944	3.166
1/qe	0.204	0.106	0.07	0.052	0.042

Table 15: Result from Desorption study

pH	Absorbance	Conc	De(mg/L)	% De
8	0.032	2.340426	2.6	10.52631579
9	0.035	2.978723	3.35	13.56275304
10	0.045	5.106383	5.85	23.68421053
11	0.067	9.787234	11.35	45.951417
12	0.044	4.893617	5.6	22.67206478
13	0.04	4.042553	4.6	18.62348178
14	0.041	4.255319	4.85	19.63562753